Appendix I

Supplementary information on Chapter 2

Figure AI.1 Displacement ellipsoid plot of $[Cu^{I}_2(\mathbf{L^3SSL^3})]^{2+}$

Table AI.1 Crystallographic data for $[Cu^{I}_2(\mathbf{L^3SSL^3})](BF_4)_2$

Table AI.2 Selected bond distances and angles of $[Cu^{I}_2(\mathbf{L^3SSL^3})](BF_4)_2$

Figure AI.2 UV-vis absorption spectra of $[Cu^{II}_2(\mathbf{L^2S})_2](BF_4)_2$ and $[Cu^{I}_2(\mathbf{L^2SSL^2})](BF_4)_2$

Figure AI.3 UV-vis absorption spectrum of $[Cu^{I}_2(\mathbf{L^4SSL^4})](BF_4)_2$

Figure AI.4 ^{1}H NMR spectra of $[Cu^{II}_2(\mathbf{L^2S})_2](BF_4)_2$ in CD_3OD at different temperatures

Figure AI.5 ^{1}H NMR spectrum of $[Cu^{II}_2(\mathbf{L^4S})_2](BF_4)_2$ in different solvents

Figure AI.6 Cyclic voltammograms of $[Cu^{II}_2(\mathbf{L^2S})_2](BF_4)_2$ and $[Cu^{II}_2(\mathbf{L^4S})_2](BF_4)_2$

Figure AI.7 Cyclic voltammograms of $[Cu^{I}_2(\mathbf{L^2SSL^2})](BF_4)_2$ and $[Cu^{I}_2(\mathbf{L^4SSL^4})](BF_4)_2$

Figure AI.8 Three optimized geometries for $[Cu^{II}_2(\mathbf{L^2S})_2]^{2+}$

Figure AI.9 Three optimized geometries for $[Cu^{II}_2(\mathbf{L^4S})_2]^{2+}$

Table AI.3 ADF total energies of all Cu^{II} μ-thiolate complexes

Table AI.4 ADF total energies of all Cu^{I} disulfide complexes

Table AI.5 ADF total energies of all copper complexes with MeCN

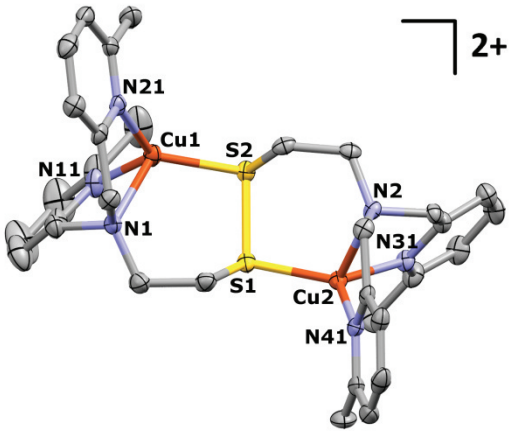

Figure AI.1: Projection of the cationic part of $[Cu^{I}_2(\mathbf{L^3SSL^3})](BF_4)_2$. Displacement ellipsoids are depicted at 50% probability level. All hydrogen atoms are omitted for clarity.

Table AI.1: Crystallographic and structure refinement data for complexes $[Cu^{I}_2(\mathbf{L^3SSL^3})](BF_4)_2$.

	$[Cu^{I}_2(\mathbf{L^3SSL^3})](BF_4)_2$
empirical formula	$[C_{32}H_{40}Cu_2N_6S_2](BF_4)_2$
formula weight	873.52
crystal system	monoclinic
space group	$P2_1/n$
a, Å	11.3108(5)
b, Å	28.8420(11)
c, Å	11.9924(4)
α, deg	90
β, deg	104.604(4)
γ, deg	90
V, Å^3	3785.8(3)
Z	4
D_{calc}, g·cm^3	1.533
T, Kelvin	110(2)
crystal size, mm	$0.21 \times 0.17 \times 0.13$
μ, mm^{-1}	1.306
no. of reflns measd	23924
no. of unique reflns	7045
no. of reflns obsd.	5654
no. of parameters	473
R_1 / wR_2 [$I > 2\sigma(I)$]	0.0431/0.0995
R_1 / wR_2 [all refl.]	0.0595/0.1059
goodness of fit	1.041
$\Delta\rho$, e·Å^{-3}	−0.50/0.78

Structure determination

All reflection intensities for $[Cu^{I}_2(\mathbf{L^3SSL^3})](BF_4)_2$ were measured at 110(2) K using a KM4/Xcalibur (detector: Sapphire3) with enhanced graphite-monochromated Mo *Kα* radiation (λ = 0.71073 Å) under the program CrysAlisPro (Version 1.171.35.11 Oxford Diffraction Ltd., 2011). The program CrysAlisPro was used to refine the cell dimensions and for data reduction. The structure was solved with the program SHELXS-97 (Sheldrick, 2008) and was refined on F^2 with SHELXL-97 (Sheldrick, 2008). Analytical numeric absorption corrections based on a multifaceted crystal model were applied using CrysAlisPro. The temperature of the data collection was controlled using the system Cryojet (manufactured by Oxford Instruments). The H atoms were placed at calculated positions using the instructions AFIX 23, AFIX 43or AFIX 137 with isotropic displacement parameters having values 1.2 or 1.5 times *U*eq of the attached C atoms.

Table AI.2: Selected bond distances and angles for $[Cu^{I}_2(\mathbf{L^3SSL^3})](BF_4)_2$.

Bond distance (Å)		**Bond angle (°)**	
Cu1 - Cu2	5.1494(6)	Cu1 - S1 - Cu2	140.21(4)
S1 - S2	2.0872(12)	Cu1 - S2 - Cu2	137.12(4)
Cu1 - S1	3.2721(8)	S1 - Cu1 - S2	38.96(3)
Cu1 - S2	2.1925(8)	S2 - Cu1 - N1	110.53(7)
Cu1 - N1	2.186(3)	S2 - Cu1 - N11	119.79(8)
Cu1 - N11	2.035(3)	S2 - Cu1 - N21	124.72(8)
Cu1 - N21	2.005(3)	N1 - Cu1 - N11	83.48(11)
Cu2 - S1	2.1901(8)	N1 - Cu1 - N21	81.83(10)
Cu2 - S2	3.3219(8)	N11 - Cu1 - N21	114.99(11)
Cu2 - N2	2.167(3)	S1 - Cu2 - S2	37.94(3)
Cu2 - N31	2.024(3)	S1 - Cu2 - N2	108.51(7)
Cu2 - N41	2.012(3)	S1 - Cu2 - N31	125.10(8)
		S1 - Cu2 - N41	116.95(8)
		N2 - Cu2 - N31	84.04(10)
Dihedral angle (°)		N2 - Cu2 - N41	81.88(10)
Cu1 - S2 - S1 - Cu2	–161.75(4)	N31 - Cu2 - N41	117.70(10)

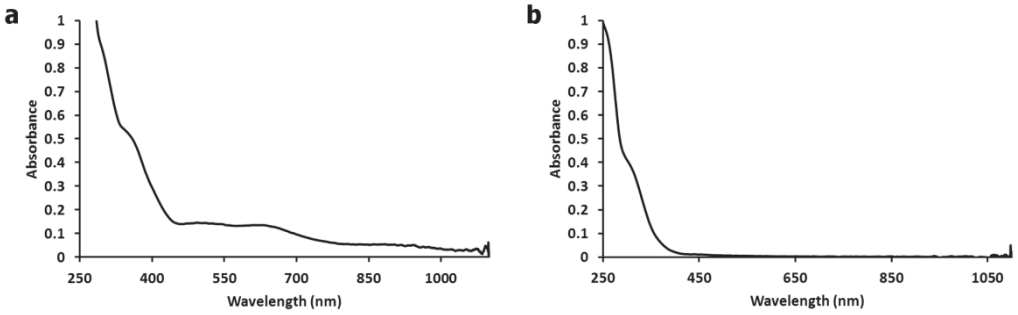

Figure AI.2: UV-vis absorption spectra of $[Cu^{II}_2(\mathbf{L^2S})_2](BF_4)_2$ (a) in dichloromethane and $[Cu^{I}_2(\mathbf{L^2SSL^2})](BF_4)_2$ (b) in acetonitrile at a concentration of 1 mM [Cu], recorded with a transmission dipprobe with a path length of 1.2 mm.

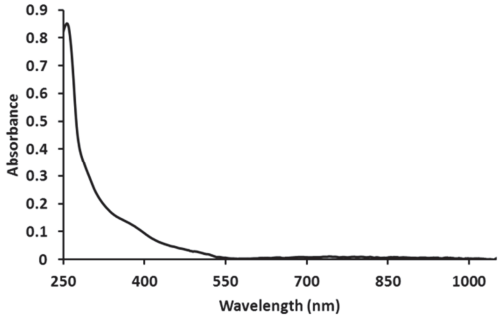

Figure AI.3: UV-vis absorption spectrum of $[Cu^{I}_2(\mathbf{L^4SSL^4})](BF_4)_2$ in methanol at a concentration of 1 mM [Cu], recorded with a transmission dipprobe with a path length of 1.2 mm.

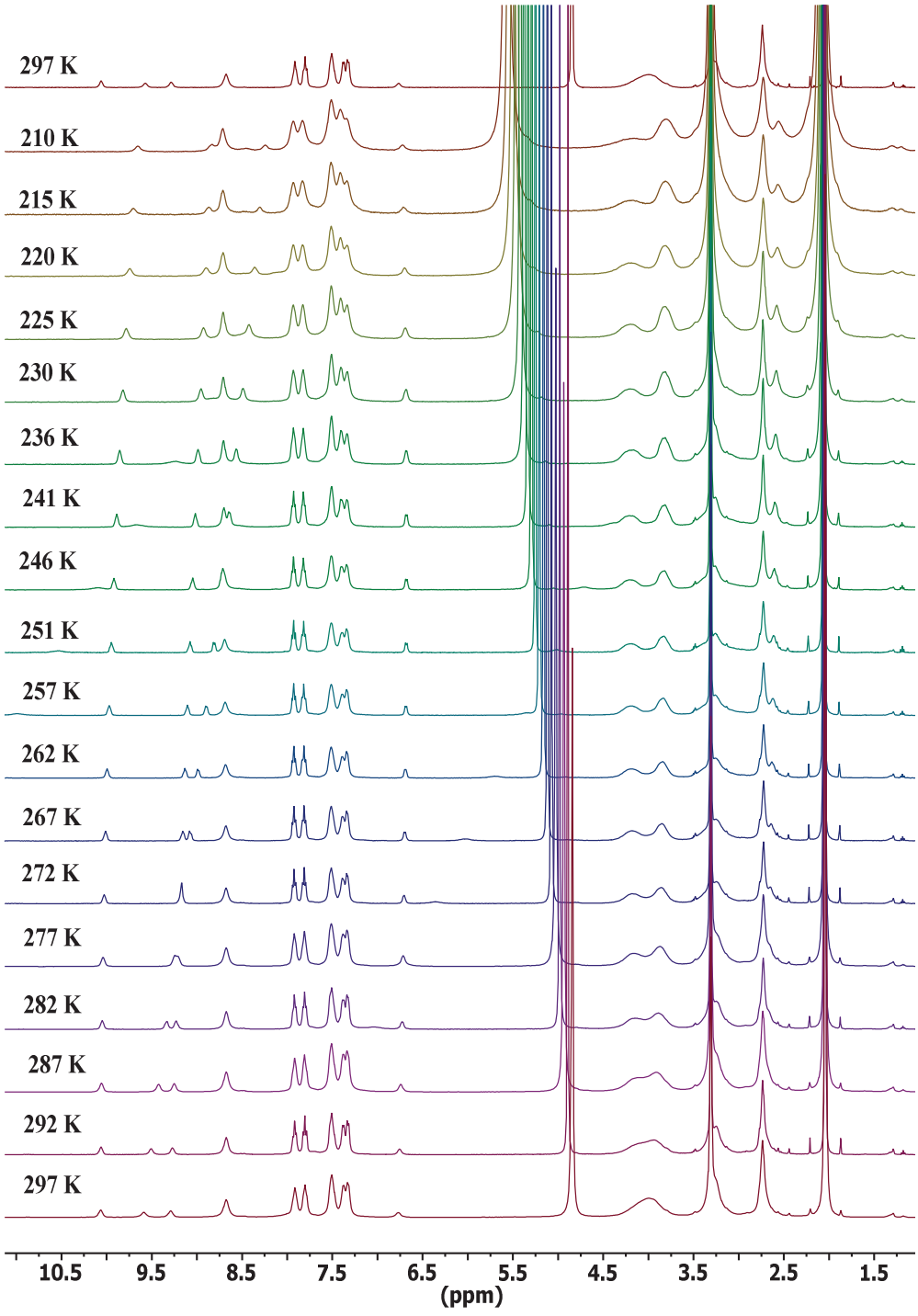

Figure AI.4: ^{1}H NMR spectra of **L^{2}SSL^{2}** and [Cu^{I}(CH$_3$CN)$_4$](BF$_4$) in CD$_3$OD measured first at 297 K, then cooled down and measured from 210 K to 297 K in steps of 5 K.

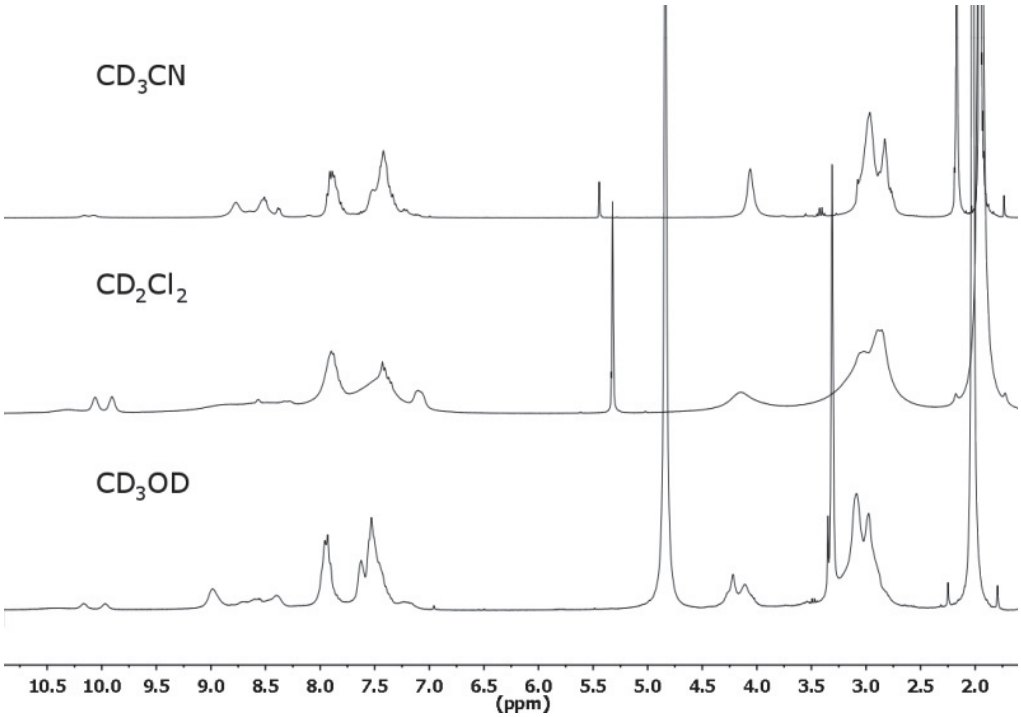

Figure AI.5: ^{1}H NMR spectra of $[Cu^{II}_2(\mathbf{L^4S})_2](BF_4)_2$ in CD_3CN, CD_2Cl_2 and CD_3OD at RT under argon.

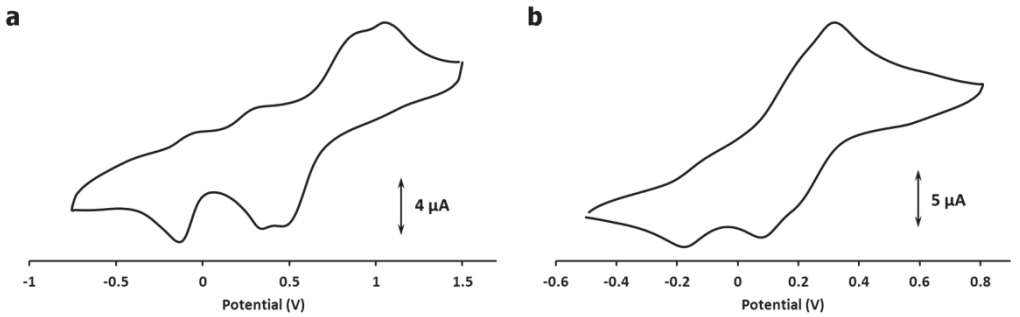

Figure AI.6: Cyclic voltammograms of (a) $[Cu^{II}_2(\mathbf{L^2S})_2](BF_4)_2$ in dichloromethane and (b) $[Cu^{II}_2(\mathbf{L^4S})_2](BF_4)_2$ in methanol at 1 mM [Cu] concentration at RT. The scanrate is 100 mV/s; potentials are given vs. Ag/AgCl.

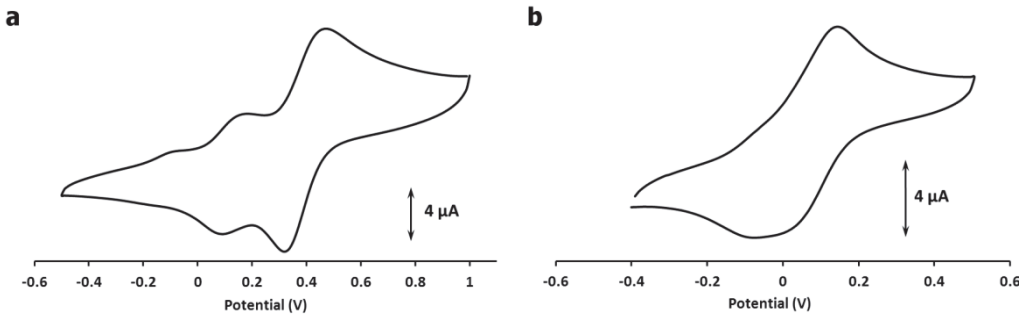

Figure AI.7: Cyclic voltammograms of (a) $[Cu^{I}_2(\mathbf{L^2SSL^2})](BF_4)_2$ in acetonitrile and (b) $[Cu^{I}_2(\mathbf{L^4SSL^4})](BF_4)_2$ in methanol at 1 mM [Cu] concentration at RT. The scanrate is 100 mV/s; potentials are given vs. Ag/AgCl.

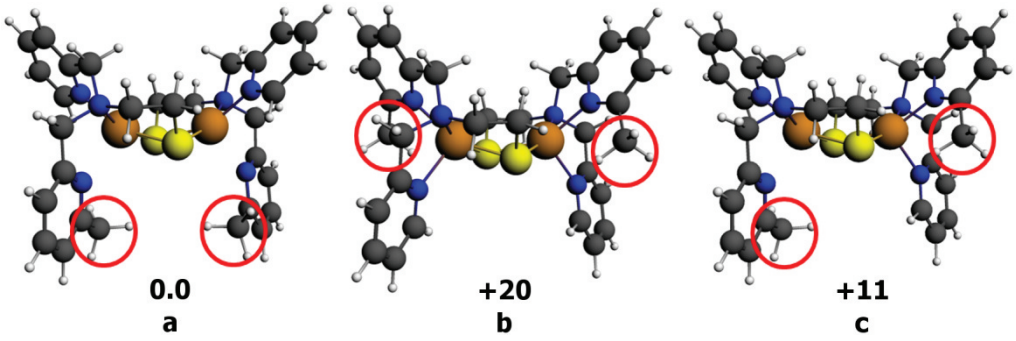

Figure AI.8: A projection of $[Cu^{II}_2(\mathbf{L^2S})_2]^{2+}$ with three different ways of coordination (a, b and c) of the two 6-methylpyridyl groups and the relative energies in kJ/mol, computed at OPBE/TZ2P in MeCN. The methyl groups are highlighted with a red circle.

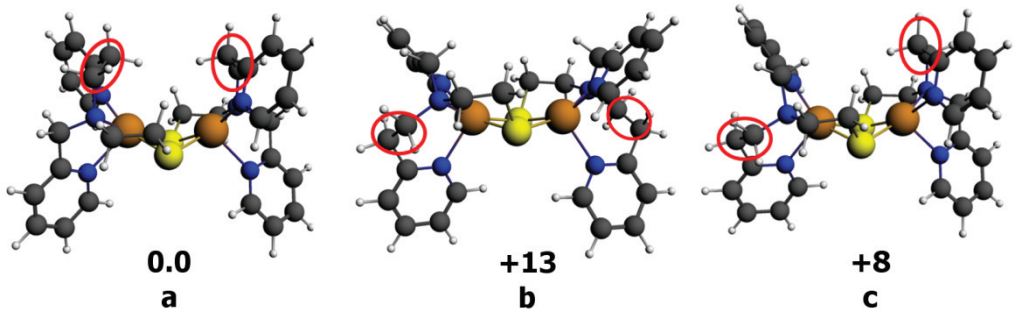

Figure AI.9: A projection of $[Cu^{II}_2(\mathbf{L^4S})_2]^{2+}$ with three different ways of coordination (a, b and c) of the two pyridyl groups with ethylene bridges and the relative energies in kJ/mol, computed at OPBE/TZ2P in MeCN. The ethylene bridges are highlighted with a red circle.

Table AI.3: ADF total energies (kJ mol^{-1}) of all Cu^{II} μ-thiolate complexes computed at ZORA-OPBE/TZ2P.

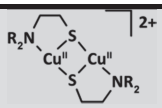 A		MeCN			gas phase		
		E_{SF}	E_1	E_0	E_{SF}	E_1	E_0
L^{1}SSL^1		–40988.3	–40986.8	–40989.9	–40493.5	–40494.2	–40492.9
L^{2}SSL^2	**a**	–44188.9	–44187.7	–44190.0	–43699.6	–43700.7	–43698.5
	b	–44171.2	–44172.7	–44169.7			
	c	–44179.7	–44180.5	–44178.9			
L^{3}SSL^3		–47375.1	–47377.2	–47373.0	–46901.0	–46904.7	–46897.2
L^{4}SSL^4	**a**	–44135.9	–44137.4	–44134.3	–43655.1	–43658.8	–43651.7
	b	–44122.0	–44122.9	–44121.0			
	c	–44128.2	–44130.1	–44126.3			
L^{5}SSL^5		–47253.1	–47257.3	–47248.9	–46785.3	–46791.1	–46779.6

Table AI.4: ADF total energies (kJ mol^{-1}) of all Cu^{I} disulfide complexes computed at ZORA-OPBE/TZ2P.

		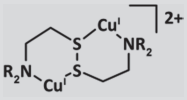 B		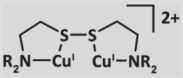 C	
		MeCN	gas phase	MeCN	gas phase
L^{1}SSL^1		–40993.5	–40509.2	–40982.9	–40507.9
L^{2}SSL^2	**a**	–44203.1	–43725.4	–44199.3	–43729.9
	b	–44205.7		–44197.2	
	c	–44204.9		–44198.9	
L^{3}SSL^3		–47412.1	–46942.7	–47406.9	–46944.2
L^{4}SSL^4	**a**	–44150.0	–43676.0	–44182.2	–43705.4
	b	–44145.7			
	c	–44148.1			
L^{5}SSL^5		–47296.2	–46835.0	–47359.1	–46898.8

Table AI.5: Energies of formation (kJ mol^{-1}) of Cu^{II} μ-thiolate (**A**) and Cu^{I} disulfide (**B** or **C**) complexes for different **LSSL** ligands with and without coordinated acetonitrile and with or without coordinated pyridyl or sulfur groups.[a]

	L^1SSL^1	**L^2SSL^2**	**L^3SSL^3**	**L^4SSL^4**	**L^5SSL^5**
A $[Cu^{II}_2(\mathbf{LS})_2]^{2+}$ + 2 CH_3CN	−80	−73	−63	−44	27
A $[Cu^{II}_2(\mathbf{LS})_2(CH_3CN)_2]^{2+}$ - N-pyr uncoordinated	x[b]	+33	+42	+87[d]	+108[d]
B $[Cu^{I}_2(\mathbf{LSSL})]^{2+}$ + 2 CH_3CN	−83	−86	−102	−60	−20
B $[Cu^{I}_2(\mathbf{LSSL})(CH_3CN)_2]^{2+}$ - N-pyr uncoordinated	−2	+10	−5	+70[d]	+26
C $[Cu^{I}_2(\mathbf{LSSL})]^{2+}$ + 2 CH_3CN	−73	−83	−97	−93	−83
C $[Cu^{I}_2(\mathbf{LSSL})(CH_3CN)_2]^{2+}$ - N-pyr uncoordinated	−6	x[c]	x[c]	−3	−19
$[Cu^{I}_2(\mathbf{LSSL})(CH_3CN)_2]^{2+}$ - S uncoordinated	−73	−79	−91[d]	−38	−20

[a] Computed at ZORA-OPBE/TZ2P in CH_3CN (COSMO).

[b] Acetonitrile dissociates from the complex

[c] Sulfur dissociates and pyridyl group re-coordinates

[d] Imaginary frequency (in the range of −23 to −134 cm^{-1}) which shows rotation of the methyl group of CH_3CN

Appendix II

Supplementary information on Chapter 3

Figure AII.1 Cyclic voltammogram of $[Cu^{I}(CH_3CN)_4](BF_4)$

Figure AII.2 UV-vis absorption spectra of $[Cu^{II}_2(\mathbf{L^{2*}S})_2](BF_4)_2$ and $[Cu^{I}_2(\mathbf{L^{2*}SSL^{2*}})](BF_4)_2$

Figure AII.3 UV-vis absorption spectra of $\mathbf{L^{1*}SSL^{1*}}$ with 0, 2 and 4 equivalents of HBF_4

Figure AII.4 UV-vis absorption spectra of $[Cu^{II}_2(\mathbf{L^{1*}S})_2]^{2+}$ with 0 - 4 equivalents of HBF_4

Figure AII.5 UV-vis absorption spectra of $[Cu^{II}_2(\mathbf{L^{1*}S})_2]^{2+}$ with 0 - 10 equivalents of HOTf

Figure AII.6 UV-vis absorption spectra of $[Cu^{II}_2(\mathbf{L^{2*}S})_2]^{2+}$ and $[Cu^{I}_2(\mathbf{L^{2*}SSL^{2*}})]^{2+}$ with 0 - 4 equivalents of HBF_4

Figure AII.7 ^1H NMR spectra of $[Cu^{II}_2(\mathbf{L^{1*}S})_2]^{2+}$ with 0, 2, 4 and 6 equivalents of HOTf

Figure AII.8 Schematic representation of the protonation of the pyridyl groups of **A**

Table AII.1 Relative geometry optimization energies of protonated **A**, **B** and **C**

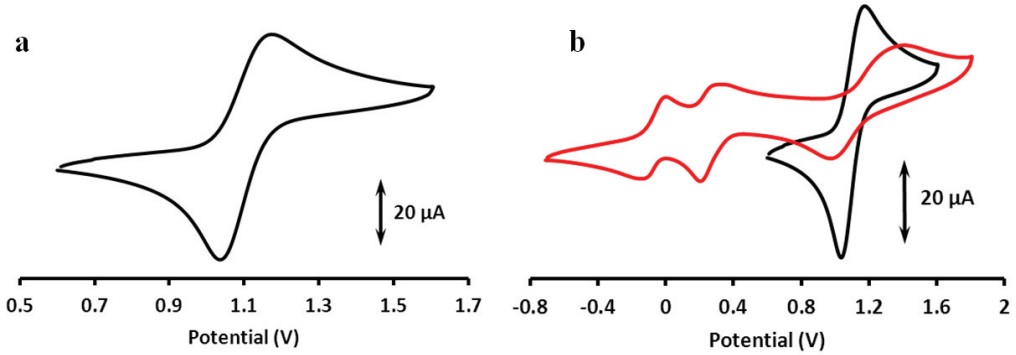

Figure AII.1: Cyclic voltammogram of $[Cu^{I}(CH_3CN)_4](BF_4)$ at a concentration of 2 mM [Cu] (a) compared with $[Cu^{I}_2Cu^{II}_2(\mathbf{L^{1*}S})_2(CH_3CN)_6]^{4+}$ (in red) at 4 mM [Cu] (b) in CH_3CN at RT. The scanrate is 100 mV/s; potentials are given vs. Ag/AgCl.

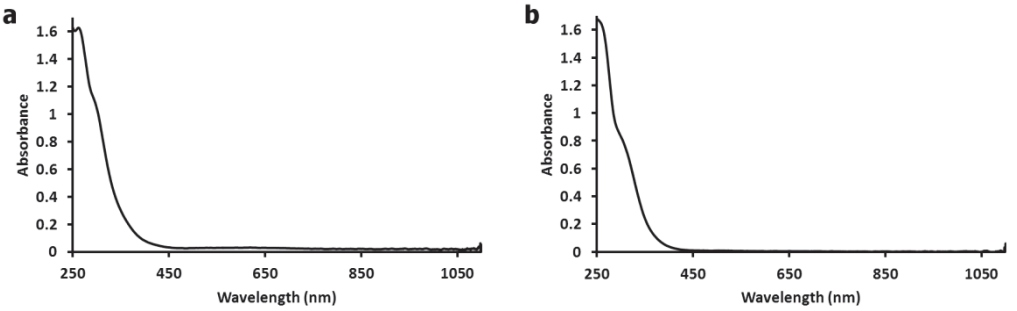

Figure AII.2: UV-vis absorption spectrum of $[Cu^{II}_2(\mathbf{L^{2*}S})_2]^{2+}$ in dichloromethane (a) and $[Cu^{I}_2(\mathbf{L^{2*}SSL^{2*}})]^{2+}$ in CH_3CN (b) at 2 mM [Cu] concentration recorded with a transmission dipprobe set at a pathlength of 1.2 mm.

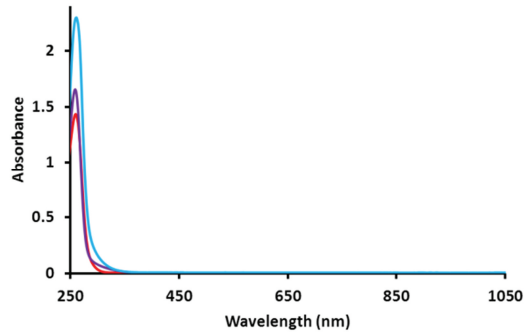

Figure AII.3: UV-vis absorption spectra of $\mathbf{L^{1*}SSL^{1*}}$ with zero (red), two (purple) and four (blue) equivalents of $HBF_4{\cdot}Et_2O$ in CH_3CN at 1 mM concentration recorded with a transmission dipprobe set at a pathlength of 1.2 mm.

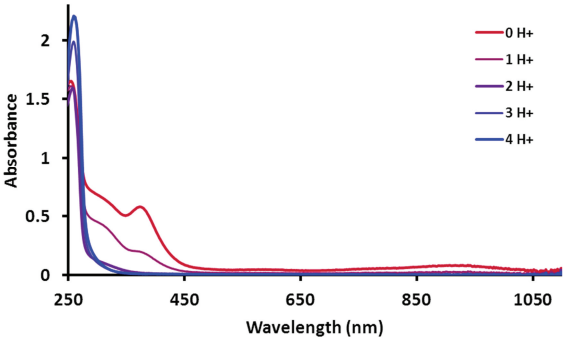

Figure AII.4: UV-vis absorption spectra of $[Cu^{II}_2(\mathbf{L^{1*}S})_2]^{2+}$ with 0 - 4 equivalents of $HBF_4{\cdot}Et_2O$ in CH_3CN at 2 mM [Cu] concentration recorded with a transmission dipprobe set at a pathlength of 1.2 mm.

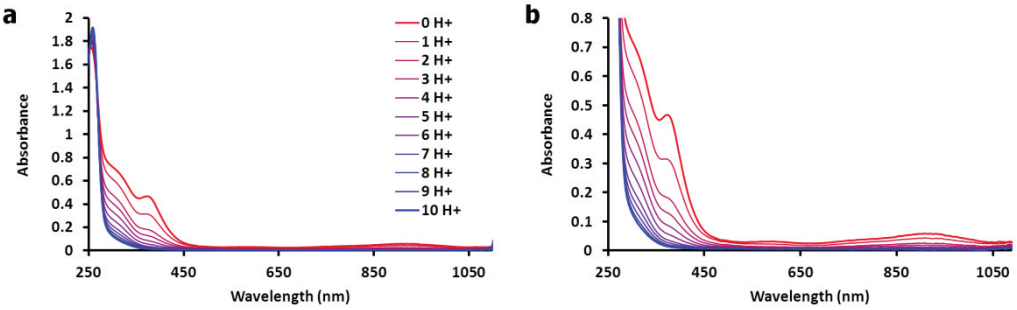

Figure AII.5: UV-vis absorption spectra of $[Cu^{II}_2(\mathbf{L^{1*}S})_2]^{2+}$ with 0 - 10 equivalents of HOTf in CH_3CN at 1 mM [Cu] concentration recorded with a transmission dipprobe set at a pathlength of 2.4 mm. (b) is a zoom of (a).

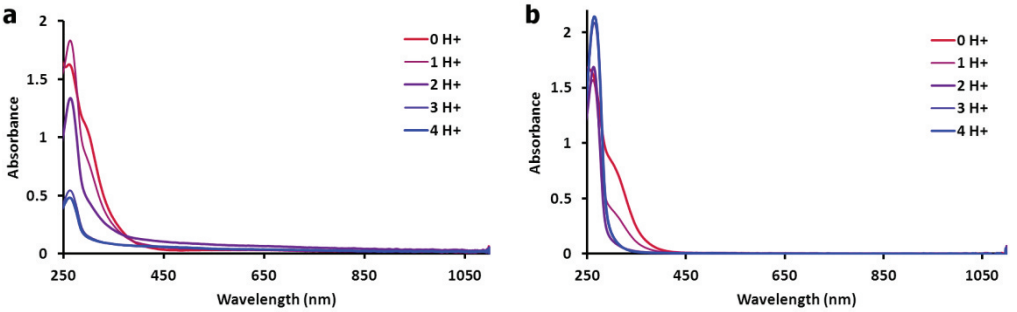

Figure AII.6: UV-vis absorption spectra of $[Cu^{II}_2(\mathbf{L^{2*}S})_2]^{2+}$ in dichloromethane (a) and $[Cu^{I}_2(\mathbf{L^{2*}SSL^{2*}})]^{2+}$ in CH_3CN (b) with 0 - 4 equivalents of $HBF_4{\cdot}Et_2O$ at 2 mM [Cu] concentration recorded with a transmission dipprobe set at a pathlength of 1.2 mm.

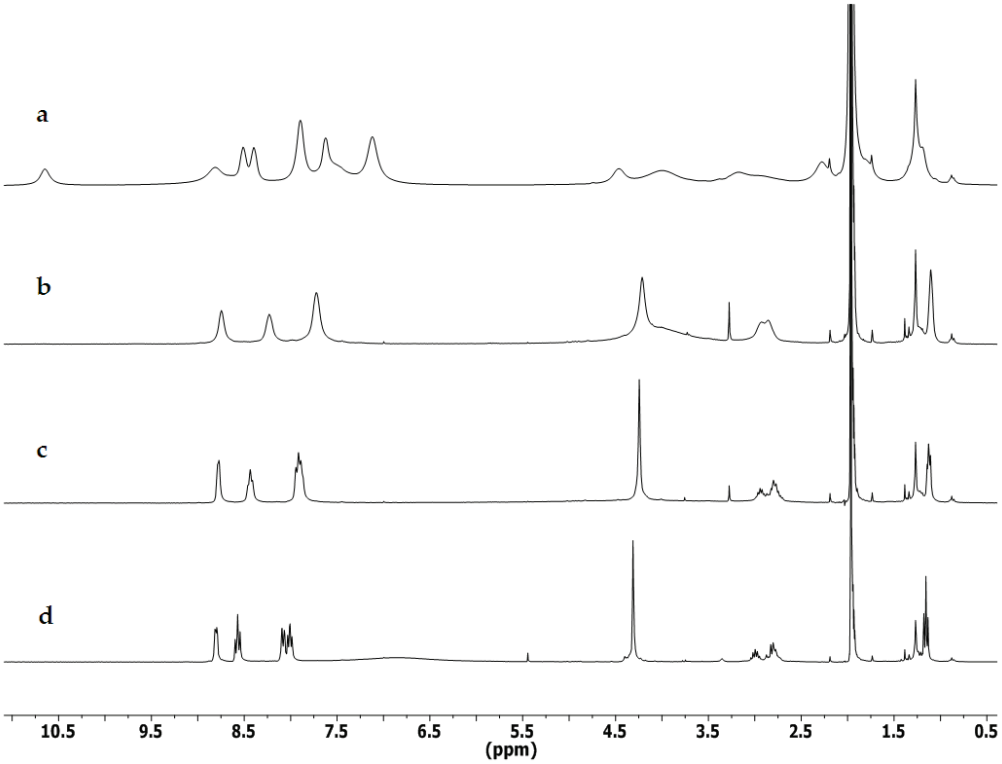

Figure AII.7: ^{1}H NMR spectra of **L^{1}*SSL^{1}*** in CD_3CN with 0 equivalents (a), 2 equivalents (b), 4 equivalents (c) and 6 equivalents (d) of HOTf at RT.

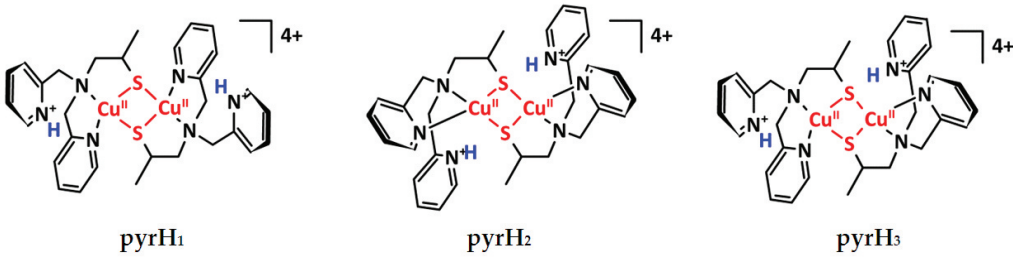

Figure AII.8: Schematic representation of three ways of protonation of two of the four pyridyl groups of $[Cu^{II}_2(\mathbf{L^{1}*S})_2]^{2+}$.

Table AII.1: Relative energies (kJ mol^{-1}) for Cu^{II} μ-thiolate (**A**) and Cu^{I} disulfide (**B** and **C**) complexes protonated in different ways (Figure AII.8) in two enantiomeric forms: *RR*/*SS* and *RS*/*SR* optimized at ZORA-OPBE/TZ2P solvated in CH_3CN (COSMO).

		X: *RR/SS*	**Z**: *RS/SR*
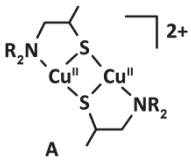 A	**A -** $pyrH_1$	**0**	18
	A - $pyrH_2$	90	25
	A - $pyrH_3$	2	19
	A - R_3NH	212	216
	A - SH	58	59
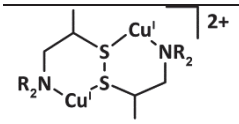 B	**B -** $pyrH_1$	54	37
	B - $pyrH_2$	46	60
	B - $pyrH_3$	27	30
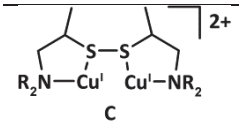 C	**C -** $pyrH_1$	57	51
	C - $pyrH_2$	58	59
	C - $pyrH_3$	78	52

Appendix III

Supplementary information on Chapter 4

Table AIII.1 Selected bond distances and angles of $[Cu^{II}_4Cu^{I}_4(\mathbf{L^{1*}S})_4(\mu\text{-}OH)_2(CH_3CN)_6](ClO_4)_6 \cdot 2\ CH_3CN$

Figure AIII.1 X-Band powder EPR spectra of $[Cu^{II}_2(\mathbf{L^{1*}SO_2})_2](BF_4)_2$ and $[Cu^{II}_2(\mathbf{L^{1*}SO_2})_2\ (OTf)_2]$

Figure AIII.2 X-Band powder EPR spectra of $Cu^{II}_2(\mathbf{L^{1*}SO_3})_2(BF_4)_2$ and $Cu^{II}_2(\mathbf{L^{1*}SO_3})_2(OTf)_2$

Figure AIII.3 X-Band EPR spectrum of $Cu^{II}_2(\mathbf{L^{1*}SO_3})_2(BF_4)_2$ dissolved in acetone

Figure AIII.4 UV-vis absorption spectra of $[Cu^{II}_2(\mathbf{L^{1*}SO_2})_2](BF_4)_2$ and $Cu^{II}_2(\mathbf{L^{1*}SO_3})_2(BF_4)_2$

Table AIII.1: Selected bond distances and angles of $[Cu^{II}_4Cu^{I}_4(\mathbf{L^{1*}S})_4(\mu\text{-}OH)_2(CH_3CN)_6](ClO_4)_6 \cdot 2\ CH_3CN$

	Bond distance (Å)		Bond angle (°)
Cu1 - S1A	2.3474(7)	S1A - Cu2 - S1D	128.55(3)
Cu2 - S1A	2.2174(8)	S1C - Cu3 - S1A	116.45(3)
Cu2 - S1D	2.2357(8)	S1B - Cu5 - S1C	129.27(3)
Cu3 - S1A	2.2967(8)	S1D - Cu6 - S1B	115.29(3)
Cu3 - S1C	2.2545(7)	O1A - Cu1 - S1A	92.93(7)
Cu4 - S1B	2.3408(8)	O1A - Cu4 - S1B	92.85(7)
Cu5 - S1B	2.2223(8)	O1B - Cu7 - S1C	93.88(6)
Cu5 - S1C	2.2257(7)	O1B - Cu8 - S1D	92.36(7)
Cu6 - S1D	2.2767(8)	Cu2 - S1A - Cu3	133.03(3)
Cu6 - S1B	2.2767(8)	Cu2 - S1A - Cu1	94.71(3)
Cu7 - S1C	2.3458(7)	Cu3 - S1A - Cu1	115.27(3)
Cu8 - S1D	2.3550(8)	Cu5 - S1B - Cu6	135.18(3)
Cu1 - O1A	1.924(2)	Cu5 - S1B - Cu4	101.19(3)
Cu4 - O1A	1.936(2)	Cu6 - S1B - Cu4	103.84(3)
Cu7 - O1B	1.909(2)	Cu5 - S1C - Cu3	117.97(3)
Cu8 - O1B	1.908(2)	Cu5 - S1C - Cu7	111.80(3)
Cu1 - N1A	2.039(2)	Cu3 - S1C - Cu7	113.15(3)
Cu1 - N11A	2.089(2)	Cu2 - S1D - Cu6	121.19(3)
Cu1 - N21A	2.118(2)	Cu2 - S1D - Cu8	115.89(3)
Cu2 - N2A	1.966(3)	Cu6 - S1D - Cu8	106.70(3)
Cu3 - N2C	2.041(3)		
Cu3 - N2B	2.077(3)		
Cu4 - N11B	2.034(3)		
Cu4 - N1B	2.047(2)		
Cu4 - N21B	2.135(2)		
Cu5 - N2D	1.964(3)		
Cu6 - N2F	2.019(3)		
Cu6 - N2E	2.092(3)		
Cu7 - N1C	2.036(2)		
Cu7 - N21C	2.083(2)		
Cu7 - N11C	2.143(2)		
Cu8 - N1D	2.031(2)		
Cu8 - N21D	2.104(2)		
Cu8 - N11D	2.129(2)		
O1A - H1H1	0.83(2)		
O1B - H1H2	0.73(2)		

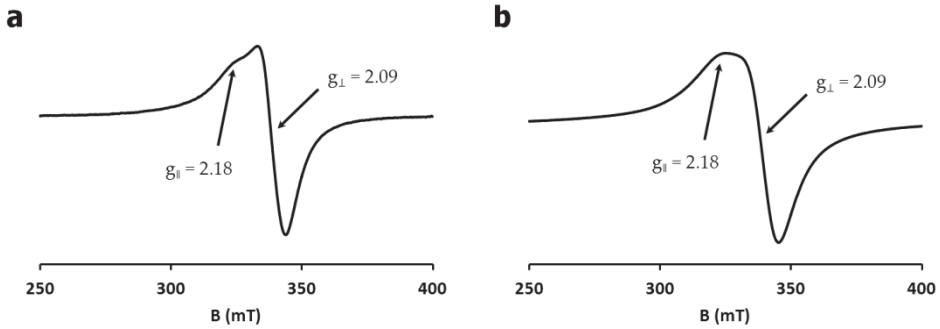

Figure AIII.1: X-Band powder EPR spectrum of $[Cu^{II}_2(\mathbf{L^{1*}SO_2})_2](BF_4)_2$ (ν = 9.881 GHz) (a) and $[Cu^{II}_2(\mathbf{L^{1*}SO_2})_2(OTf)_2]$ (ν = 9.883 GHz) (b) at RT.

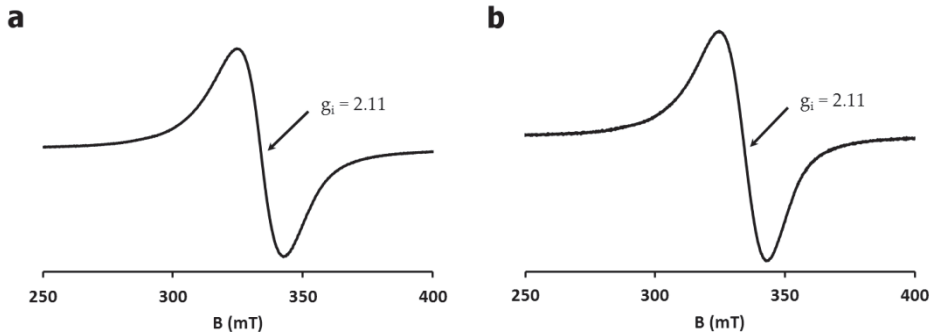

Figure AIII.2: X-Band powder EPR spectrum of $Cu^{II}_2(\mathbf{L^{1*}SO_3})_2(BF_4)_2$ (ν = 9.879 GHz) (a) and $Cu^{II}_2(\mathbf{L^{1*}SO_3})_2(OTf)_2$ (ν = 9.878 GHz) (b) at RT.

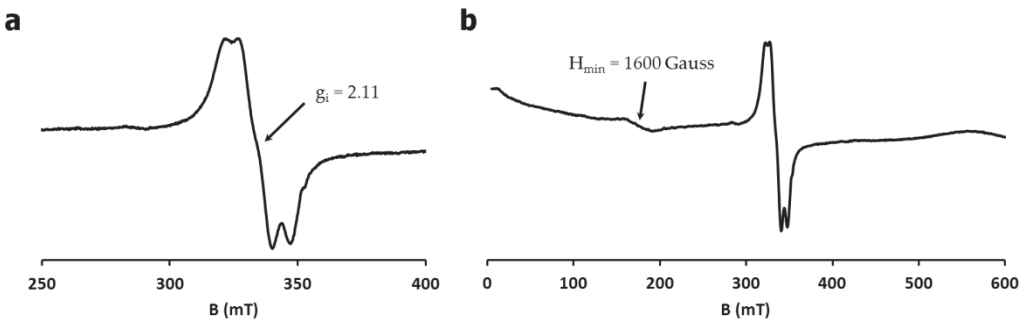

Figure AIII.3: X-Band EPR spectrum of $Cu^{II}_2(\mathbf{L^{1*}SO_3})_2(BF_4)_2$ dissolved in acetone (ν = 9.873 GHz) at RT depicted from 250 to 400 mT (a) and 0 to 600 mT (b).

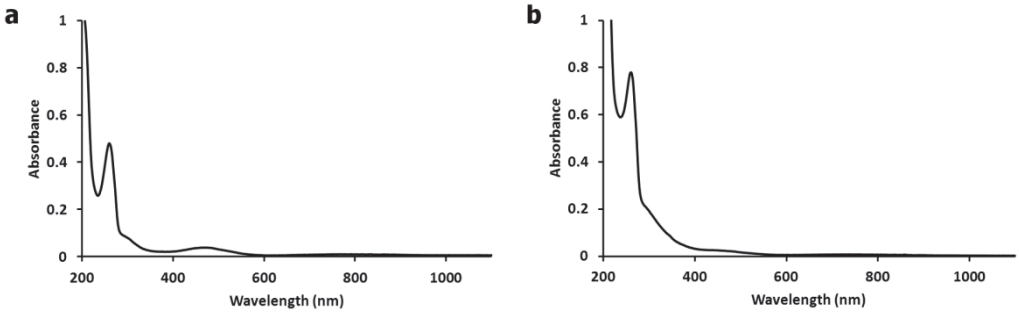

Figure AIII.4: UV-vis absorption spectra of $[Cu^{II}_2(\mathbf{L^{1*}SO_2})_2](BF_4)_2$ (a) and $Cu^{II}_2(\mathbf{L^{1*}SO_3})_2(BF_4)_2$ (b) at a concentration of 0.1 mM [Cu] in acetonitrile, recorded with a path length of 10 mm.

Appendix IV

Supplementary information on Chapter 5

Figure AIV.1 Displacement ellipsoid plot of **L^{1}SXSL^1**

Figure AIV.2 Displacement ellipsoid plot of [Cu$^{II}_2$(**L^{MPz}SSL^{MPz}**)(Cl)$_2$]$_n$(BF$_4$)$_{2n}$

Table AIV.1 Crystallographic data for **L^{1}SXSL^1** and [Cu$^{II}_2$(**L^{MPz}SSL^{MPz}**)(Cl)$_2$]$_n$(BF$_4$)$_{2n}$

Table AIV.2 Selected bond distances and angles for [Cu$^{II}_2$(**L^{MPz}SSL^{MPz}**)(Cl)$_2$]$_n$(BF$_4$)$_{2n}$

Figure AIV.3 ^{1}H NMR spectra of **L^{1}SXSL^1** and [Cu$^{I}_2$(**L^{1}SXSL^1**)(CH$_3$CN)](BF$_4$)$_2$

Figure AIV.4 ^{1}H NMR spectra of **L^{Pz}SSL^{Pz}** and [Cu$^{I}_2$(**L^{Pz}SSL^{Pz}**)](BF$_4$)$_2$

Figure AIV.5 ^{1}H NMR spectra of **L^{MPz}SSL^{MPz}** and [Cu$^{I}_2$(**L^{MPz}SSL^{MPz}**)](BF$_4$)$_2$

Figure AIV.6 Cyclic voltammograms of [Cu$^{I}_2$(**L^{Pz}SSL^{Pz}**)](BF$_4$)$_2$

Figure AIV.7 Cyclic voltammograms of [Cu$^{I}_2$(**L^{MPz}SSL^{MPz}**)](BF$_4$)$_2$

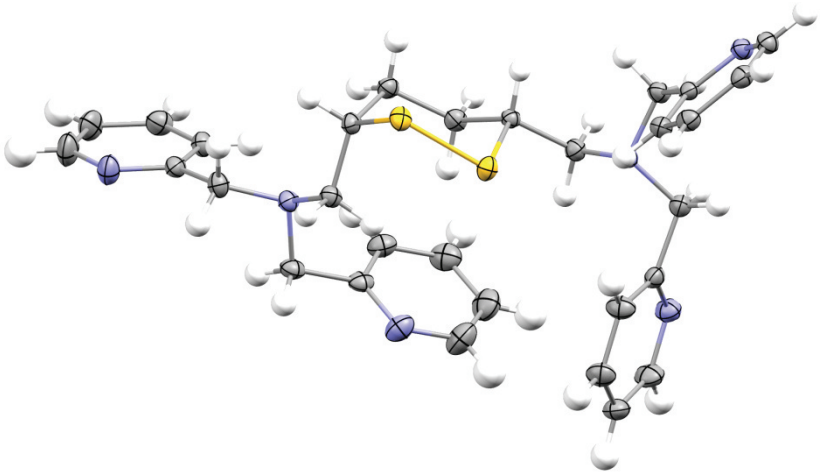

Figure AIV.1: Displacement ellipsoid plot (50% probability level) of **L^{1}SXSL^{1}**.

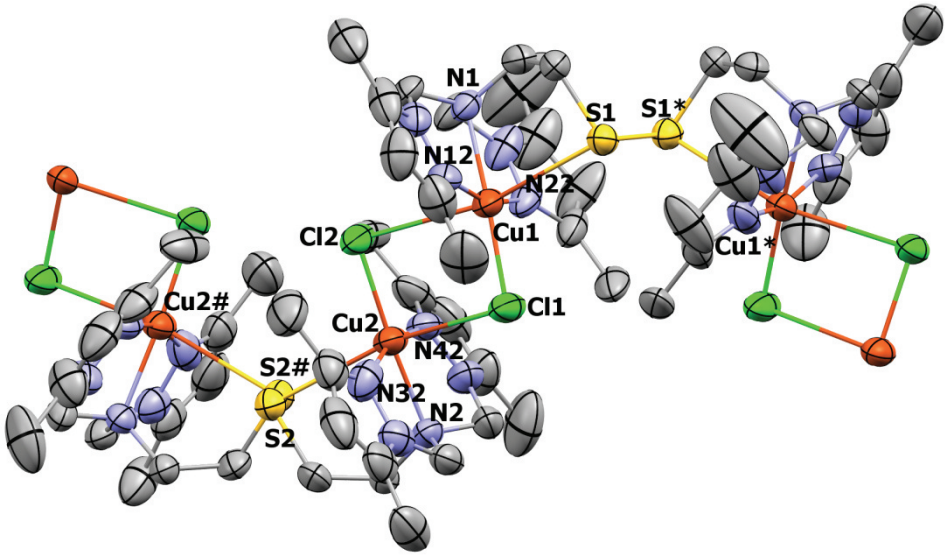

Figure AIV.2: Displacement ellipsoid plot (50% probability level) of $[Cu^{II}_2(\mathbf{L}^{MPz}\mathbf{SSL}^{MPz})(Cl)_2]_n(BF_4)_{2n}$. Hydrogen atoms, counterions and lattice solvent molecules are omitted for clarity. Symmetry operation * = [1–x, y, ½–z] and # = [–x, y, ½–z]

Synthesis of $[Cu^{II}_2(\mathbf{L^{MPz}SSL^{MPz}})(Cl)_2]_n(BF_4)_{2n}$

$\mathbf{L^{MPz}SSL^{MPz}}$ (0.103 g, 0.18 mmol) was dissolved in 5 mL CH_3CN. To this solution $[Cu^{II}(H_2O)_6](BF_4)_2$ (0.062 g, 0.18 mmol) and $CuCl_2 \cdot 2\ H_2O$ (0.032 g, 0.18 mmol) were added and the mixture was stirred for 10 minutes. Diethyl ether (10 mL) was added, which resulted in a precipitate that was filtered and washed with diethyl ether giving $[Cu^{II}_2(\mathbf{L^{MPz}SSL^{MPz}})(Cl)_2]_n(BF_4)_{2n}$ (0.130 g, 0.14 mmol, 76%) as a light green powder. ESI-MS found (calculated) for $[M - 2\ BF_4]^{2+}$ *m*/*z* 391.0 (391.1); $[½\ M - Cl - BF_4]^+$ *m*/*z* 355.0 (355.1); $[½\ M - BF_4 + Cl]^+$ *m*/*z* 426.9 (427.0). IR (neat, cm^{-1}): 2999*w*, 1553*m*, 1477*m*, 1418*m*, 1392*m*, 1280*m*, 1048*vs*, 1020*vs*, 1006*s*, 912*m*, 797*m*, 624*m*, 521*m* 468*m*. Elemental analysis calcd for $[Cu^{II}_2(\mathbf{L^{MPz}SSL^{MPz}})(Cl)_2](BF_4)_2$: C 35.16, H 4.64, N 14.64, S 6.70; Found: C 33.92, H 4.50, N 14.34, S 6.27. UV-vis in CH_3CN at 0.1 mM [Cu] concentration: 213 nm (18 000 $M^{-1}\ cm^{-1}$), 285 nm (ε = 3 300 $M^{-1}\ cm^{-1}$), 750 nm (ε = 100 $M^{-1}\ cm^{-1}$). X-band powder EPR spectrum (RT, ν = 9.855 GHz): g_{iso} = 2.10; X-band EPR spectrum in CH_3CN (RT, ν = 9.865 GHz): g_{iso} = 2.10.

Table AIV.1: Crystallographic and structure refinement data for $\mathbf{L^1SXSL^1}$ and $[Cu^{II}_2(\mathbf{L^{MPz}SSL^{MPz}})(Cl)_2]_n(BF_4)_{2n}$.

	$\mathbf{L^1SXSL^1}$	$[Cu^{II}_2(\mathbf{L^{MPz}SSL^{MPz}})(Cl)_2]_n(BF_4)_{2n}$
empirical formula	$C_{30}H_{34}N_6S_2$	$[C_{28}H_{44}Cl_2Cu_2N_{10}S_2](BF_4)_2 \cdot CH_3CN$
formula weight	542.75	994.48
crystal system	triclinic	monoclinic
space group	*P*-1	*C*2/*c*
a, Å	6.1886(2)	16.0760(4)
b, Å	14.4574(5)	30.5905(3)
c, Å	16.6963(5)	19.2993(5)
α, deg	104.490(3)	90
β, deg	98.618(3)	114.138(3)
γ, deg	95.211(3)	90
V, Å^3	1417.08(8)	8661.0(4)
Z, *Z'*	2, 1	8, 1
D_{calc}, g·cm^3	1.272	1.525
T, Kelvin	100(2)	110(2)
crystal size, mm	$0.27 \times 0.09 \times 0.06$	$0.53 \times 0.41 \times 0.34$
μ, mm^{-1}	1.933	3.885
no. of reflns measd	16387	30710
no. of unique reflns	5554	8476
no. of reflns obsd.	5229 [$I > 2\sigma(I)$]	7664 [$I > 2\sigma(I)$]
no. of parameters	343	689
R_1 / wR_2 [$I > 2\sigma(I)$]	0.0406/0.0984	0.0737/0.2156
R_1 / wR_2 [all refl.]	0.0432/0.1000	0.0789/0.2241
goodness of fit	1.118	1.056
$\Delta\rho$, e·Å^{-3}	−0.26 /0.50	−0.84 /1.09

Structure determination

The reflection intensities for **L^{1}SXSL^1** and [Cu$^{II}_2$(**L^{MPz}SSL^{MPz}**)(Cl)$_2$]$_n$(BF$_4$)$_{2n}$ were measured using a SuperNova diffractometer (equipped with Atlas detector) with Cu *K*α radiation (λ = 1.54178 Å) under the program CrysAlisPro (Versions 1.171.36.24 or 1.171.36.32 Agilent Technologies, 2012-2013). The same program was used to refine the cell dimensions and for data reduction. The structure was solved with the program SHELXS-2013 (Sheldrick, 2013) and was refined on F^2 with SHELXL-2013 (Sheldrick, 2013). Analytical numeric absorption correction based on a multifaceted crystal model was applied using CrysAlisPro. The temperature of the data collection was controlled using the system Cryojet (manufactured by Oxford Instruments). The H atoms were placed at calculated positions using the instructions AFIX 13, AFIX 23, AFIX 43 or AFIX 137 with isotropic displacement parameters having values 1.2 or 1.5 times *U*eq of the attached C atoms.

For [Cu$^{II}_2$(**L^{MPz}SSL^{MPz}**)(Cl)$_2$]$_n$(BF$_4$)$_{2n}$ the structure was solved and refined in the space group *C*2/*c*, and is found to be polymeric along the **a** direction with the repeating unit corresponding to the dicopper(II) complex $C_{28}H_{44}Cl_2Cu_2N_{10}S_2$. A first check with ADDSYM in Platon (Spek, 2003) suggests a *C*2/*c* to *Fddd* transformation *via* the transformation matrix (1 0 0 / 0 –1 0 / –1 0 –2), but such a transformation remains unlikely as the β angle would be *ca.* 90.47°. The space group *C*2/*c* remains the most likely space group as there are no strong evidences for wrong space group assignment (0 Systematic absence violations, 10 Inconsistent equivalents, *R*(int) = 0.0268, R(sigma) = 0.0201). The implementation of the twin matrix (–1 0 0 / 0 –1 0 / 1 0 1) (found *via* TwinRotMat in Platon) helps to drop the *R*1 factor a bit, and the BASF scale factor refines to 0.369(5). In the structure, the polymeric unit remains ordered while all counterions and lattice solvent molecules are significantly disordered. Two BF_4^- counterions are found at sites of twofold axial symmetry, and are constrained to be disordered with an occupancy factor of 0.5 for each counterion. The remaining BF_4^- counterion is found at no special position, but is disordered over 4 different orientations, whose occupancy factors refine to 0.314(3), 0.202(3), 0.230(3) and 0.254(3) (the SUMP instruction was used so that the sum of the four occupancy factors equals to 1). In the asymmetric unit, there is one lattice acetonitrile solvent molecule, which is found very disordered. Modelling of the disorder is very approximate (as it is likely that the molecule is disordered over more than 2 orientations), and the occupancy factor of the major component refines to 0.702(15). The H atoms of the very disordered acetonitrile lattice solvent molecule have been omitted in the final refinement. A SQUEEZE refinement was not possible as the different components of the disorder are close to the very disordered BF_4^- counterion.

Table AIV.2: Selected bond distances and angles for $[Cu^{II}_2(\mathbf{L^{MPz}SSL^{MPz}})(Cl)_2]_n(BF_4)_{2n}$.

Bond distance (Å)		Bond angle (°)	
Cu1 - Cu2	3.6500(15)	S1 - Cu1 - N1	81.24(19)
S1 - S1*	2.052(3)	S1 - Cu1 - N12	83.7(2)
S2 - S2#	2.046(4)	S1 - Cu1 - N22	92.5(2)
Cu1 - S1	2.977(2)	S1 - Cu1 - Cl2	163.74(7)
Cu1 - N1	2.124(5)	N1 - Cu1 - N12	81.3(2)
Cu1 - N12	1.986(6)	N1 - Cu1 - N22	80.4(2)
Cu1 - N22	1.967(7)	N1 - Cu1 - Cl1	176.13(17)
Cu1 - Cl1	2.235(2)	N12 - Cu1 - N22	161.7(3)
Cu1 - Cl2	2.895(3)	S2 - Cu2 - N2	81.57(19)
Cu2 - S1	2.972(2)	S2 - Cu2 - N32	83.1(2)
Cu2 - N2	2.083(5)	S2 - Cu2 - N42	93.8(2)
Cu2 - N32	1.963(8)	S2 - Cu2 - Cl1	164.65(7)
Cu2 - N42	1.968(7)	N2 - Cu2 - N32	81.4(3)
Cu2 - Cl1	2.899(3)	N2 - Cu2 - N42	82.4(2)
Cu2 - Cl2	2.402(19)	N2 - Cu2 - Cl2	176.35(18)
		N32 - Cu2 - N42	163.8(3)

Symmetry operation * = [1–x, y, ½–z], # = [–x, y, ½–z]

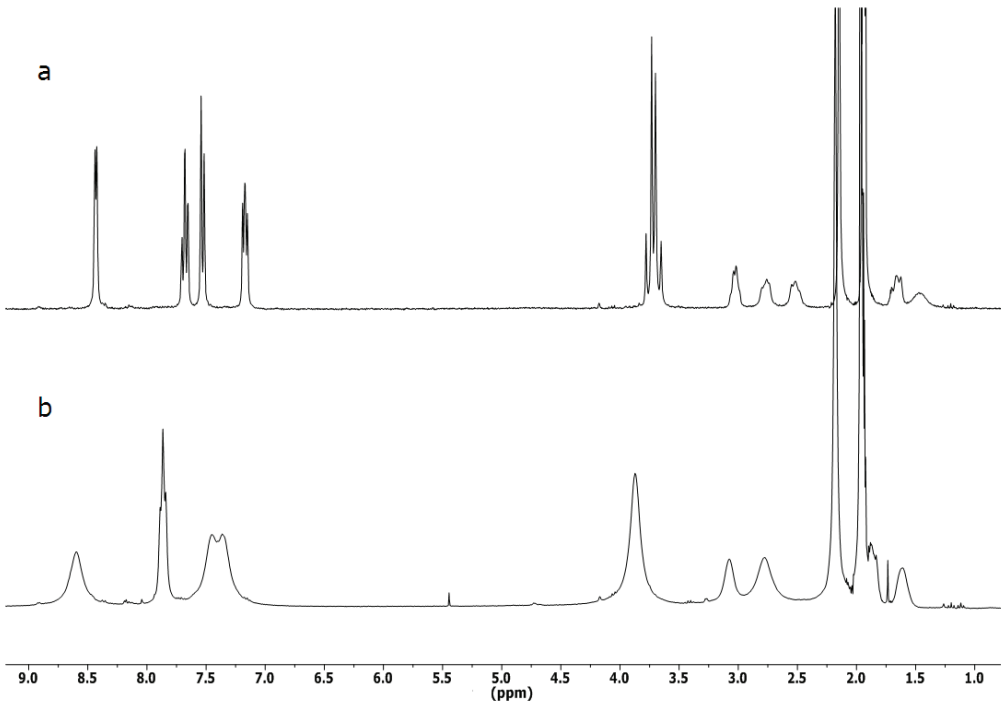

Figure AIV.3: ^{1}H NMR spectra of $\mathbf{L^1SXSL^1}$ (a) and $[Cu^I_2(\mathbf{L^1SXSL^1})(CH_3CN)](BF_4)_2$ (b) in CD_3CN.

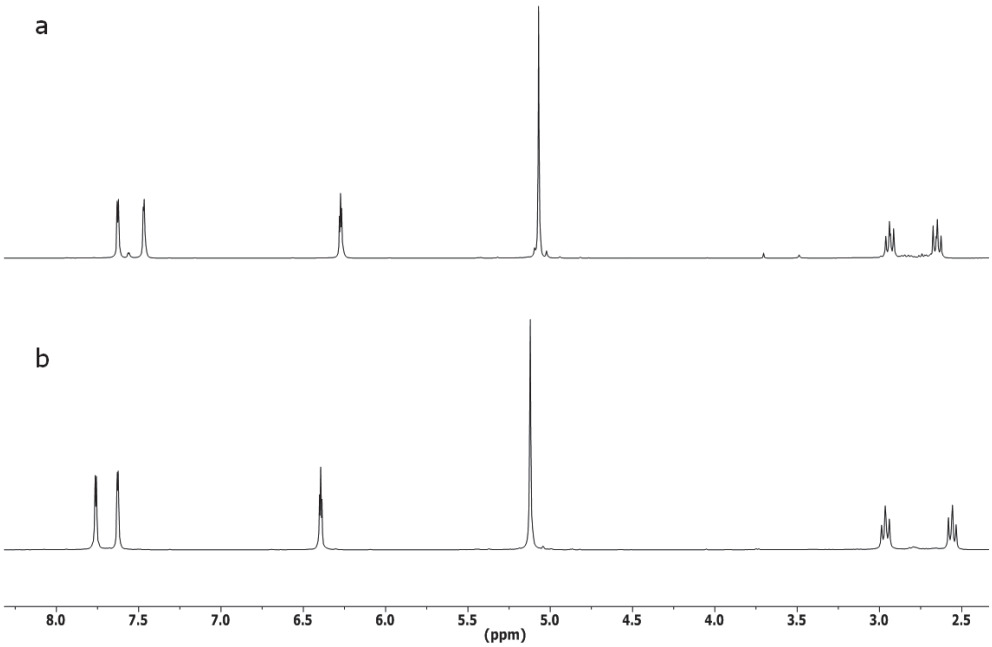

Figure AIV.4: ^{1}H NMR spectra of $\mathbf{L^{Pz}SSL^{Pz}}$ (a) and $[Cu^{I}_{2}(\mathbf{L^{Pz}SSL^{Pz}})](BF_4)_2$ (b) in CD_3CN.

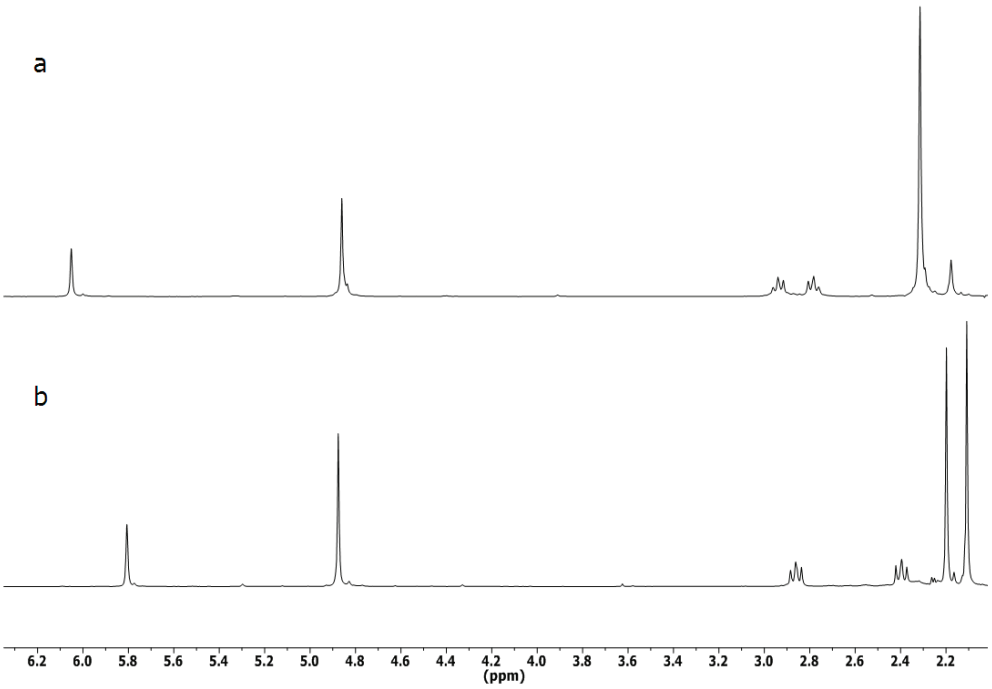

Figure AIV.5: ^{1}H NMR spectra of $\mathbf{L^{MPz}SSL^{MPz}}$ (a) and $[Cu^{I}_{2}(\mathbf{L^{MPz}SSL^{MPz}})](BF_4)_2$ (b) in CD_3CN.

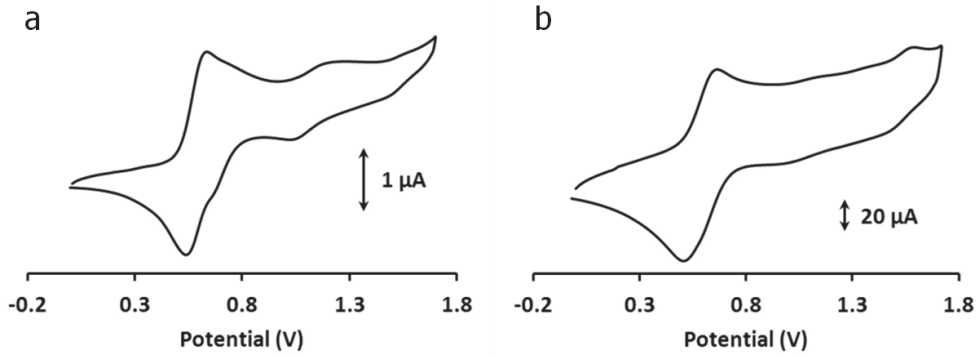

Figure AIV.6: Cyclic voltammograms of $[Cu^{I}_2(\mathbf{L^{Pz}SSL^{Pz}})](BF_4)_2$ in acetonitrile at 20 mV/s (a) and 1000 mV/s (b) at 2.0 mM [Cu] concentration. Potentials are given vs Ag/AgCl.

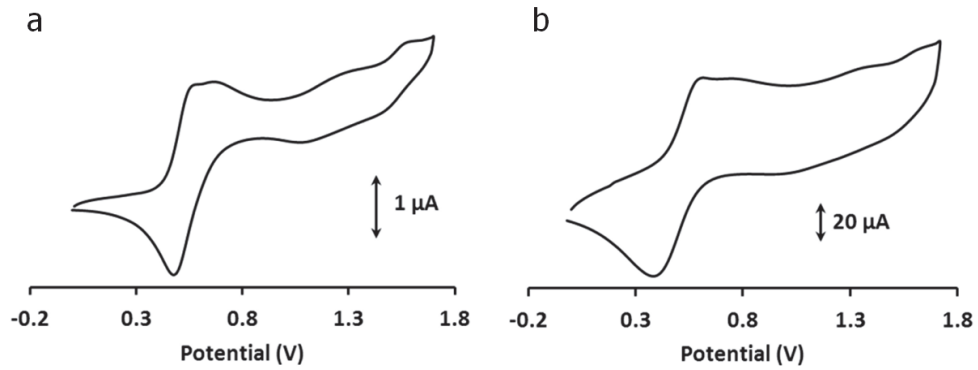

Figure AIV.7: Cyclic voltammograms of $[Cu^{I}_2(\mathbf{L^{MPz}SSL^{MPz}})](BF_4)_2$ in acetonitrile at 20 mV/s (a) and 1000 mV/s (b) at 2.0 mM [Cu] concentration. Potentials are given vs Ag/AgCl.

Appendix V

Supplementary information on Chapter 6

Figure AV.1 Raman spectra of $[Cu^{II}(\mathbf{L^1SCH_3})(OPh\text{-}X)]^+$ with different X substituents

Figure AV.2 X-band EPR spectrum of $[Cu^{II}(\mathbf{L^1SCH_3})(OPh)](SbF_6)$

Figure AV.3 Cyclic voltammograms of $[Cu^{II}(\mathbf{L^1SCH_3})(OPh\text{-}Me)](OTf)$ at different scanrates

Figure AV.4 Cyclic voltammograms of $[Cu^{II}(\mathbf{L^1SCH_3})(OPh\text{-}Me)](OTf)$ with different potential ranges

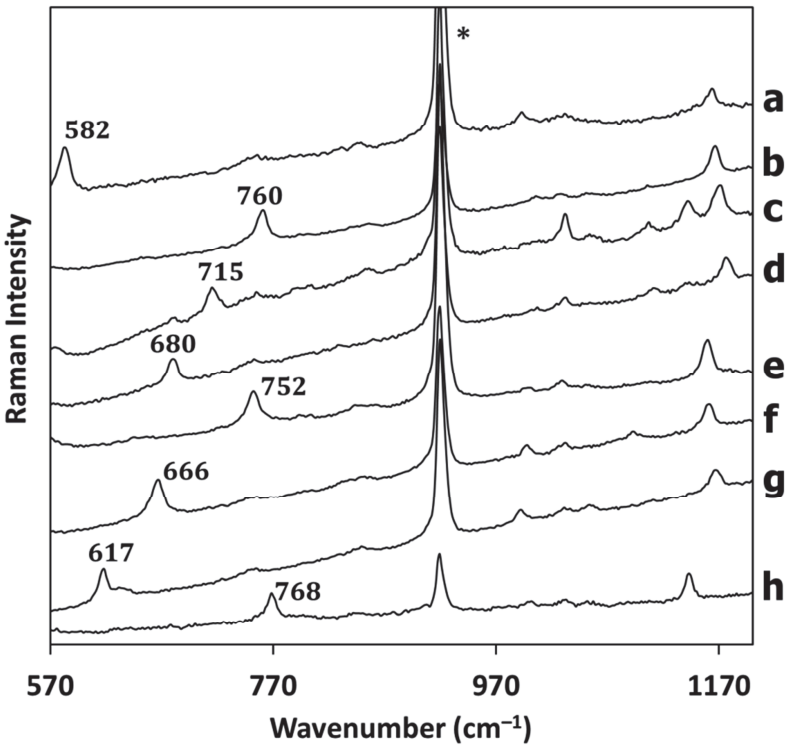

Figure AV.1: Raman spectra of $[Cu^{II}(\mathbf{L^1SCH_3})]^{2+}$ coordinated to X-PhO^- with different substituents on the *para*-position; X = (a) H, (b), CH_3, (c) *iso*-propyl, (d) *tert*-butyl, (e) OCH_3, (f) Cl, (g) I and (h) F. Spectra were recorded on a confocal Raman microscope at an excitation wavelength of 532 nm with 2 s exposure time. The spectra are the average of 25 accumulations. * = CH_3CN

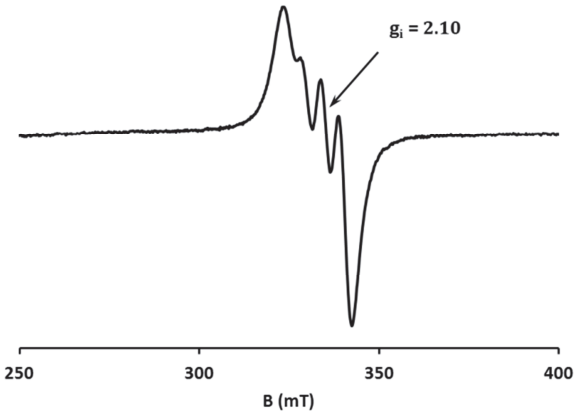

Figure AV.2: X-band EPR spectrum (ν = 9.863 GHz) of $[Cu^{II}(\mathbf{L^1SCH_3})(OPh)](SbF_6)$ at RT dissolved in CH_3CN; $g_i = 2.10$, $A_i = 52$ Gauss.

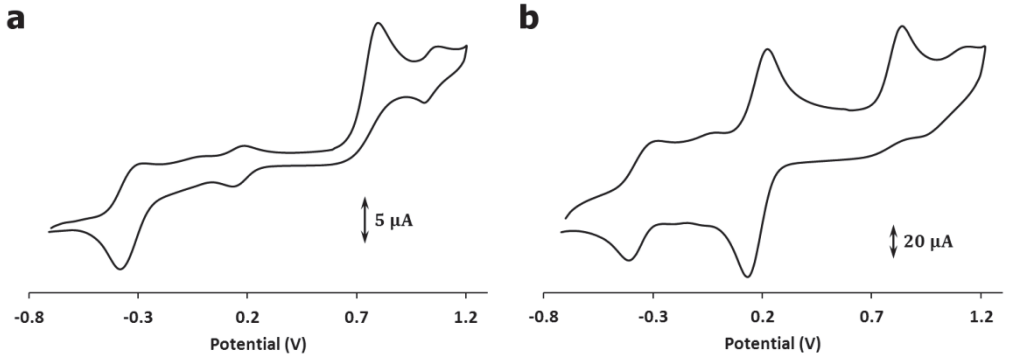

Figure AV.3: Cyclic voltammograms of [Cu^{II}(**L^1SCH_3**)(OPh-Me)](OTf) measured at a scanrate of (a) 20 mV/s and (b) 1000 mV/s in CH_3CN at 2.0 mM [Cu] concentration. Potentials are given vs Ag/AgCl.

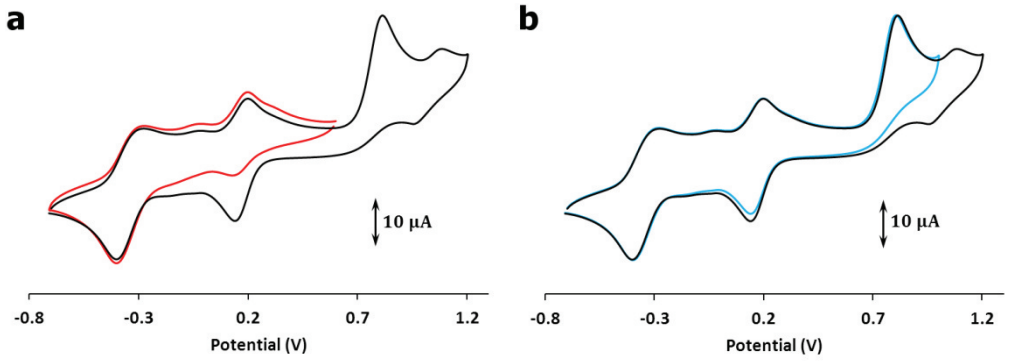

Figure AV.4: Cyclic voltammograms of [Cu^{II}(**L^1SCH_3**)(OPh-Me)](OTf) measured in a potential range of (a) –0.7 to 1.2 V (black) and –0.7 to 0.6 V (red); (b) –0.7 V to 1.2 V (black) and –0.7 to 1.0 V (blue) at a scanrate of 100 mV/s in CH_3CN at 2.0 mM [Cu] concentration. Potentials are given vs Ag/AgCl.

Appendix VI

Supplementary information on Chapter 7

Figure AVI.1 Displacement ellipsoid plots of $[Cu^{II}_2(\mathbf{L^1SSL^1})(Cl)_2]_n(BF_4)_{2n}$ and $[Cu^{II}_2(\mathbf{L^2SSL^2})(Cl)_2]_n(ClO_4)_{2n}$

Figure AVI.2 Displacement ellipsoid plots of $[Cu^{II}(\mathbf{L^1{*}SCH_3})(Cl)](BF_4)$ and $[Cu^{II}(\mathbf{L^1{*}SCH_3})(Cl)]_2(CuCl_4)$

Table AVI.1 Crystallographic data for $[Cu^{II}_2(\mathbf{L^1SSL^1})(Cl)_2]_n(BF_4)_{2n}$, $[Cu^{II}_2(\mathbf{L^2SSL^2})(Cl)_2]_n(ClO_4)_{2n}$, $[Cu^{II}(\mathbf{L^1{*}SCH_3})(Cl)](BF_4)$ and $[Cu^{II}(\mathbf{L^1{*}SCH_3})(Cl)]_2(CuCl_4)$

Table AVI.2 Selected bond distances and angles for $[Cu^{II}_2(\mathbf{L^1SSL^1})(Cl)_2]_n(BF_4)_{2n}$, $[Cu^{II}_2(\mathbf{L^2SSL^2})(Cl)_2]_n(ClO_4)_{2n}$, $[Cu^{II}(\mathbf{L^1{*}SCH_3})(Cl)](BF_4)$ and $[Cu^{II}(\mathbf{L^1{*}SCH_3})(Cl)]_2(CuCl_4)$

Figure AVI.3 UV-vis spectra of synthesized Cu^{II} complexes

Figure AVI.4 UV-vis spectra of 3,5-DTBQ formation catalyzed by $[Cu^{II}_2(\mathbf{L^{Pz}SSL^{Pz}})(Cl)_2]_n(BF_4)_{2n}$

Figure AVI.5 UV-vis spectra of $[Cu^{II}_2(\mathbf{L^{Pz}SSL^{Pz}})](BF_4)_4$ in the presence of different amounts of chlorides

Figure AVI.6 Absorption curves at 400 nm of 3,5-DTBQ formation catalyzed by $[Cu^{II}_2(\mathbf{L^{Pz}SSL^{Pz}})](BF_4)_4$ in the presence of different amounts of chlorides

Figure AVI.7 Absorption curves at 400 nm of 3,5-DTBQ formation catalyzed by $[Cu^{II}_2(\mathbf{L^1{*}SSL^{1*}})](BF_4)_4$ at different catalyst concentrations

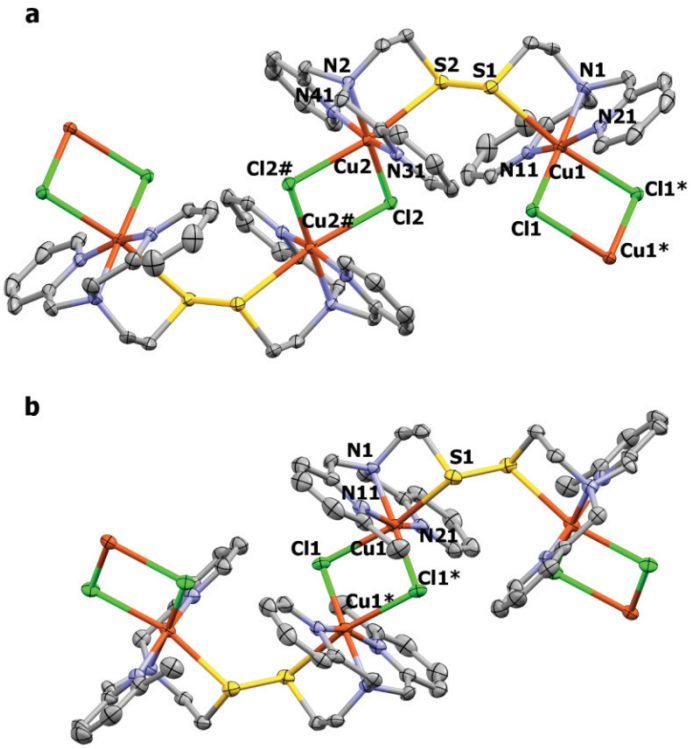

Figure AVI.1: Displacement ellipsoid plots (50% probability level) of (a) $[Cu^{II}_2(\mathbf{L^1SSL^1})(Cl)_2]_n(BF_4)_{2n}$ and (b) $[Cu^{II}_2(\mathbf{L^2SSL^2})(Cl)_2]_n(ClO_4)_{2n}$. Hydrogen atoms, lattice solvent molecules (only for $[Cu^{II}_2(\mathbf{L^1SSL^1})(Cl)_2]_n(BF_4)_{2n}$) and non-coordinating counterions are omitted for clarity. Symmetry operation * = [–x, 1–y, 1–z] and # = [–x, 1–y, –z] for $[Cu^{II}_2(\mathbf{L^1SSL^1})(Cl)_2]_n(BF_4)_{2n}$. Symmetry operation * = [1–x, 2–y, –z] for $[Cu^{II}_2(\mathbf{L^2SSL^2})(Cl)_2]_n(ClO_4)_{2n}$.

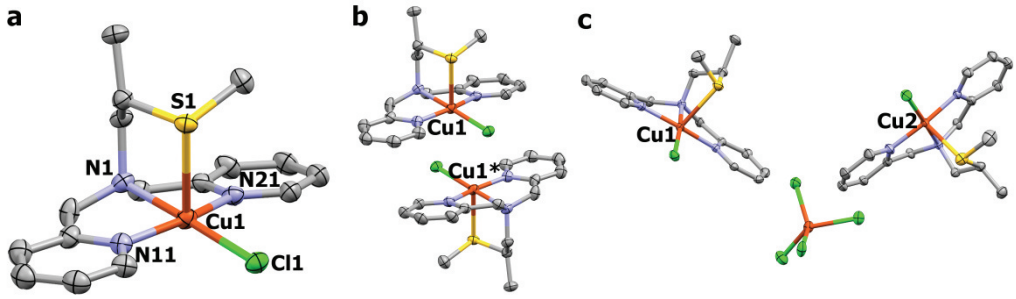

Figure AVI.2: Displacement ellipsoid plots (50% probability level) of one (a) and two (b) cationic subunits of $[Cu^{II}(\mathbf{L^{1*}SCH_3})(Cl)](BF_4)$ and of (c) $[Cu^{II}(\mathbf{L^{1*}SCH_3})(Cl)]_2(Cu^{II}Cl_4)$. Disorder (only for $[Cu^{II}(\mathbf{L^{1*}SCH_3})(Cl)](BF_4)$), hydrogen atoms and BF_4^- counterions have been omitted for clarity. Symmetry operation * = [2–x, –y, 1–z].

*Synthesis of [Cu^{II}(**L^1*SCH$_3$**)(Cl)]$_2$(CuCl$_4$)*

L^1*SCH$_3$ (690 mg; 2.40 mmol) and Cu^{II}Cl$_2$ · 2 H$_2$O (614 mg; 3.60 mmol) were dissolved in 50 mL methanol and refluxed for 1 hour. The solution was cooled down and left to evaporate until green crystals had formed. The crystals were filtered and washed with methanol and diethyl ether to give [Cu^{II}(**L^1*SCH$_3$**)(Cl)]$_2$(CuCl$_4$) (789 mg; 0.807 mmol; 67%). Crystals suitable for X-ray structure determination were originally obtained from 1 instead of 1.5 equiv of Cu^{II}Cl$_2$ · 2 H$_2$O. ESI-MS found (calculated) for [½ M – CuCl$_4$]$^+$ *m*/*z* 384.8 (385.0). IR (neat, cm^{-1}): 2932*w*, 1607*s*, 1573*w*, 1482*m*, 1440*s*, 1299*m*, 1284*m*, 1157*m*, 1053*m*, 1030*s*, 989*w*, 938*w*, 868*m*, 770*s*, 728*w*, 656*w*, 420*s*. Elemental analysis calcd for [Cu^{II}(**L^1*SCH$_3$**)(Cl)]$_2$(CuCl$_4$): C 39.29, H 4.33, N 8.59, S 6.56; Found: C 38.61, H 4.39, N 8.39, S 6.49. UV-vis in CH$_3$CN at 0.15 mM [Cu] concentration: 259 nm (ε = 12 100 M^{-1} cm^{-1}), 305 nm (ε = 5 100 M^{-1} cm^{-1}), 464 nm (ε = 750 M^{-1} cm^{-1}), 700 nm (ε = 130 M^{-1} cm^{-1}), 890 nm (ε = 190 M^{-1} cm^{-1}).

Structure Determination

The reflection intensities for [Cu^{II}(**L^1*SCH$_3$**)(Cl)](BF$_4$) were measured at 110(2) K using a SuperNova diffractometer (equipped with Atlas detector) with Cu *Kα* radiation (*λ* = 1.54178 Å) under the program CrysAlisPro (Version 1.171.36.32 Agilent Technologies, 2013). The same program was used to refine the cell dimensions and for data reduction. The structure was solved with the program SHELXS-2013 (Sheldrick, 2013) and was refined on F^2 with SHELXL-2013 (Sheldrick, 2013). Analytical numeric absorption corrections based on a multifaceted crystal model were applied using CrysAlisPro. The temperature of the data collection was controlled using the system Cryojet (manufactured by Oxford Instruments). The H atoms were placed at calculated positions using the instructions AFIX 13, AFIX 23, AFIX 43, AFIX 137 or AFIX 147 with isotropic displacement parameters having values 1.2 or 1.5 times *U*eq of the attached C atoms.

The reflection intensities for [Cu$^{II}_2$(**L^{1}SSL^1**)(Cl)$_2$]$_n$(BF$_4$)$_{2n}$, [Cu$^{II}_2$(**L^{2}SSL^2**)(Cl)$_2$]$_n$(ClO$_4$)$_{2n}$ and [Cu^{II}(**L^1*SCH$_3$**)(Cl)]$_2$(CuCl$_4$) were measured using a KM4/Xcalibur (detector: Sapphire3) with enhanced graphite-monochromated Mo *Kα* radiation (*λ* = 0.71073 Å) at 110(2) K under the program CrysAlisPro (Version 1.171.35.11 or 1.171.36.24 Agilent Technologies, 2011-2012). The same program was used to refine the cell dimensions and for data reduction. The structures were solved with the program SHELXS-97 (Sheldrick, 2008) and was refined on F^2 with SHELXL-97 (Sheldrick, 2008). Analytical numeric absorption corrections based on a multifaceted crystal model were applied using CrysAlisPro. The temperature of the data collection was controlled using the system Cryojet (manufactured by Oxford Instruments). The H atoms were placed at calculated positions using the instructions AFIX 13, AFIX 23, AFIX 43 or AFIX 137 with isotropic displacement parameters having 1.2 or 1.5 times *U*eq of the attached C atoms.

Table AVI.1: Crystallographic and structure refinement data for complexes $[Cu^{II}_2(\mathbf{L^1SSL^1})(Cl)_2]_n(BF_4)_{2n}$, $[Cu^{II}_2(\mathbf{L^2SSL^2})(Cl)_2]_n(ClO_4)_{2n}$, $[Cu^{II}(\mathbf{L^1{*}SCH_3})(Cl)](BF_4)$ and $[Cu^{II}(\mathbf{L^1{*}SCH_3})(Cl)]_2(CuCl_4)$.

	$[Cu^{II}_2(\mathbf{L^1SSL^1})(Cl)_2]_n(BF_4)_{2n}$	$[Cu^{II}_2(\mathbf{L^2SSL^2})(Cl)_2]_n(ClO_4)_{2n}$	$[Cu^{II}(\mathbf{L^1{*}SCH_3})(Cl)](BF_4)$	$[Cu^{II}(\mathbf{L^1{*}SCH_3})(Cl)]_2(CuCl_4)$
empirical formula	$[C_{28}H_{32}Cl_2Cu_2N_6S_2](BF_4)_2 \cdot 2\,CH_3CN$	$[C_{15}H_{18}ClCuN_3S](ClO_4)$	$[C_{16}H_{21}ClCuN_3S](BF_4)$	$[C_{16}H_{21}ClCuN_3S]_2(CuCl_4)$
formula weight	970.42	470.82	473.22	978.16
crystal system	triclinic	monoclinic	monoclinic	monoclinic
space group	*P*-1	*C*2/*c*	$P2_1/c$	$P2_1/n$
a, Å	12.4006(2)	21.2487(5)	13.4189(4)	13.6254(3)
b, Å	13.1923(3)	12.6146(2)	12.5086(3)	13.2651(3)
c, Å	14.4294(4)	14.6206(4)	12.8357(5)	22.7359(5)
α, deg	104.022(2)	90	90	90
β, deg	107.238(2)	110.200(3)	116.644(4)	102.954(2)
γ, deg	99.5150(18)	90	90	90
V, Å^3	2114.51(8)	3677.92(16)	1925.71(12)	4004.76(15)
Z	2	8	4	4
D_{calc}, g·cm^3	1.524	1.701	1.632	1.622
T, K	110(2)	110(2)	110(2)	110(2)
crystal size, mm	0.57×0.42×0.26	0.19×0.19×0.17	0.17×0.12×0.02	0.52×0.35×0.15
μ, mm^{-1}	1.301	1.618	4.297	2.116
no. of reflns measd	28931	13583	13585	27367
no. of unique reflns	9699	3708	3754	8080
no. of reflns obsd.	8706 [$I > 2\sigma(I)$]	3303 [$I > 2\sigma(I)$]	3206 [$I > 2\sigma(I)$]	6596 [$I > 2\sigma(I)$]
no. of parameters	669	282	294	446
R_1 / wR_2 [$I > 2\sigma(I)$]	0.0231/0.0620	0.0361/0.0930	0.0368/0.0889	0.0447/0.1218
R_1 / wR_2 [all refl.]	0.0266/0.0630	0.0413/0.0955	0.0455/0.0930	0.0573/0.1290
goodness of fit	1.074	1.058	1.041	1.051
$\Delta\rho$, e·Å^{-3}	−0.31/0.33	−0.39/0.87	−0.27/0.60	−1.08/2.62

Table AVI.2: Selected bond distances (Å) and bond angles (°) for complexes $[Cu^{II}_2(\mathbf{L^1SSL^1})(Cl)_2]_n(BF_4)_{2n}$, $[Cu^{II}_2(\mathbf{L^2SSL^2})(Cl)_2]_n(ClO_4)_{2n}$, $[Cu^{II}(\mathbf{L^{1*}SCH_3})(Cl)](BF_4)$ and $[Cu^{II}(\mathbf{L^{1*}SCH_3})(Cl)]_2(CuCl_4)$.

	$[Cu^{II}_2(\mathbf{L^1SSL^1})(Cl)_2]_n(BF_4)_{2n}$	$[Cu^{II}_2(\mathbf{L^2SSL^2})(Cl)_2]_n(ClO_4)_{2n}$	$[Cu^{II}(\mathbf{L^{1*}SCH_3})(Cl)](BF_4)$	$[Cu^{II}(\mathbf{L^{1*}SCH_3})(Cl)]_2(CuCl_4)$
Cu1 - Cu1*	3.5955(3)	3.6455(4)	3.7751(6)	3.9085(7)
Cu2 - Cu2#	3.6192(3)			
Cu1 - Cu2/Cu1#	5.6586(3)	5.6416(5)		
Cu1 - S1	2.8896(4)	2.7676(7)	2.645(3)	2.6608(11)
Cu1 - N1	2.0523(12)	2.041(2)	2.054(2)	2.054(3)
Cu1 - N11	1.9803(12)	2.074(2)	2.003(2)	1.987(3)
Cu1 - N21	1.9901(12)	2.028(2)	2.001(2)	1.985(3)
Cu1 - Cl1	2.2666(4)	2.2644(7)	2.2662(7)	2.2594(10)
Cu1 - Cl1*	2.7862(4)	2.7428(8)	3.0985(8)	3.2663(12)
Cu2 - S2	2.8619(4)			
Cu2 - N2	2.0601(12)			
Cu2 - N31	1.9713(11)			
Cu2 - N41	1.9868(12)			
Cu2 - Cl2	2.2693(3)			
Cu2 - Cl2#	2.7719(3)			
S1 - Cu1 - N1	84.11(4)	85.43(7)	86.52(8)	85.49(9)
S1 - Cu1 - N11	92.75(4)	77.40(7)	86.43(8)	102.36(10)
S1 - Cu1 - N21	87.29(4)	100.67(7)	101.32(8)	86.22(9)
S1 - Cu1 - Cl1/Cl1*	170.50(1)	164.24(2)	96.32(6)	101.22(4)
N1 - Cu1 - N11	81.65(5)	82.10(9)	82.86(9)	81.61(13)
N1 - Cu1 - N21	83.23(5)	81.20(9)	81.80(9)	84.00(13)
N1 - Cu1 - Cl1	179.10(4)	174.37(7)	177.11(6)	173.26(9)
N11 - Cu1 - N21	164.80(5)	163.29(9)	162.32(9)	162.57(14)
S2 - Cu2 - N2	83.68(3)			
S2 - Cu2 - N31	93.92(4)			
S2 - Cu2 - N41	85.95(4)			
S2 - Cu2 - Cl2#	171.24(1)			
N2 - Cu2 - N31	82.10(5)			
N2 - Cu2 - N41	83.37(5)			
N2 - Cu2 - Cl2	179.11(4)			
N31 - Cu2 - N41	165.39(5)			

Symmetry operation * = [–x, 1–y, 1–z] for $[Cu^{II}_2(\mathbf{L^1SSL^1})(Cl)_2]_n(BF_4)_{2n}$; [1–x, 2–y, –z] for $[Cu^{II}_2(\mathbf{L^2SSL^2})(Cl)_2]_n(ClO_4)_{2n}$; [2–x, –y, 1–z] for $[Cu^{II}(\mathbf{L^{1*}SCH_3})(Cl)](BF_4)$; [1–x, 1–y, –z] for $[Cu^{II}(\mathbf{L^{1*}SCH_3})(Cl)]_2(CuCl_4)$. Symmetry operation # = [–x, 1–y, –z] for $[Cu^{II}_2(\mathbf{L^1SSL^1})(Cl)_2]_n(BF_4)_{2n}$; [1–x, y, ½–z] for $[Cu^{II}_2(\mathbf{L^2SSL^2})(Cl)_2]_n(ClO_4)_{2n}$.

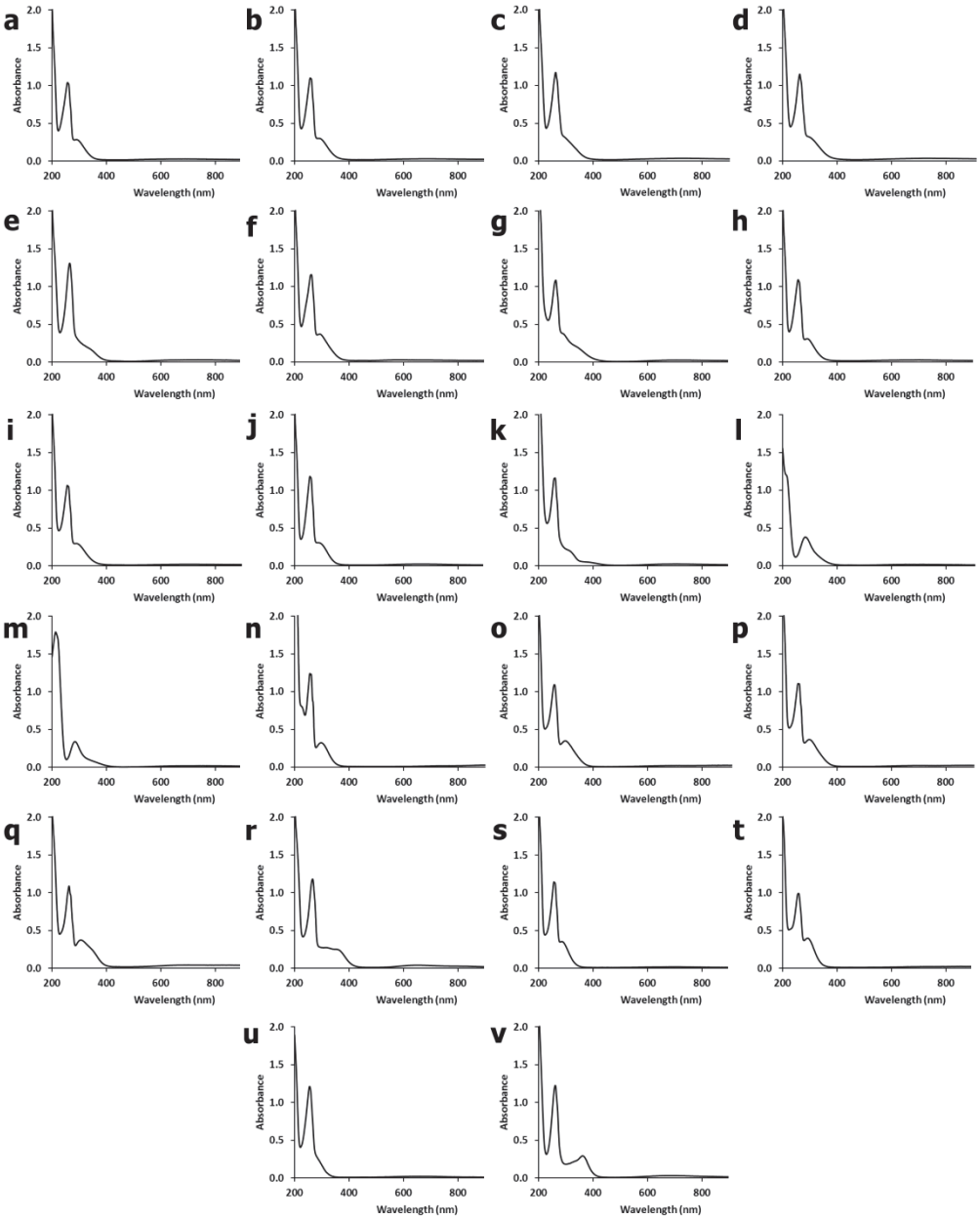

Figure AVI.3: UV-vis spectra of (a) $[Cu^{II}_2(\mathbf{L^1SSL^1})(Cl)_2]_n(BF_4)_{2n}$, (b) $[Cu^{II}_2(\mathbf{L^{1*}SSL^{1*}})(Cl)_2]_n(BF_4)_{2n}$, (c) $[Cu^{II}_2(\mathbf{L^2SSL^2})(Cl)_2]_n(BF_4)_{2n}$, (d) $[Cu^{II}_2(\mathbf{L^{2*}SSL^{2*}})(Cl)_2]_n(BF_4)_{2n}$, (e) $[Cu^{II}_2(\mathbf{L^3SSL^3})(Cl)_2]_n(BF_4)_{2n}$, (f) $[Cu^{II}_2(\mathbf{L^4SSL^4})(Cl)_2]_n(BF_4)_{2n}$, (g) $[Cu^{II}_2(\mathbf{L^5SSL^5})(Cl)_2]_n(BF_4)_{2n}$, (h) $[Cu^{II}_2(\mathbf{L^1SXSL^1})(Cl)_2]_n(BF_4)_{2n}$, (i) $[Cu^{II}_2(\mathbf{L^1SL^1})(Cl)_2]_n(BF_4)_{2n}$, (j) $[Cu^{II}_2(\mathbf{L^1C_6L^1})(Cl)_2]_n(BF_4)_{2n}$, (k) $[Cu^{II}_2(\mathbf{L^1PhL^1})(Cl)_2]_n(BF_4)_{2n}$, (l) $[Cu^{II}_2(\mathbf{L^{Pz}SSL^{Pz}})(Cl)_2]_n(BF_4)_{2n}$, (m) $[Cu^{II}_2(\mathbf{L^{MPz}SSL^{MPz}})(Cl)_2]_n(BF_4)_{2n}$, (n) $[Cu^{II}(\mathbf{Py_3N})(Cl)](BF_4)$, (o) $[Cu^{II}(\mathbf{L^1SCH_3})(Cl)](BF_4)$, (p) $[Cu^{II}(\mathbf{L^{1*}SCH_3})(Cl)](BF_4)$, (q) $[Cu^{II}(\mathbf{L^2SCH_3})(Cl)](BF_4)$, (r) $[Cu^{II}(\mathbf{L^3SCH_3})(Cl)](BF_4)$, (s) $[Cu^{II}(\mathbf{L^1OH})(Cl)](BF_4)$, (t) $[Cu^{II}(\mathbf{L^1NH_2})(Cl)](BF_4)$, (u) $[Cu^{II}(\mathbf{Py_2NH})(Cl)](BF_4)$ and (v) $[Cu^{II}(\mathbf{Py_2S})(Cl)](BF_4)$ in CH_3CN at 0.1 mM [Cu] concentration.

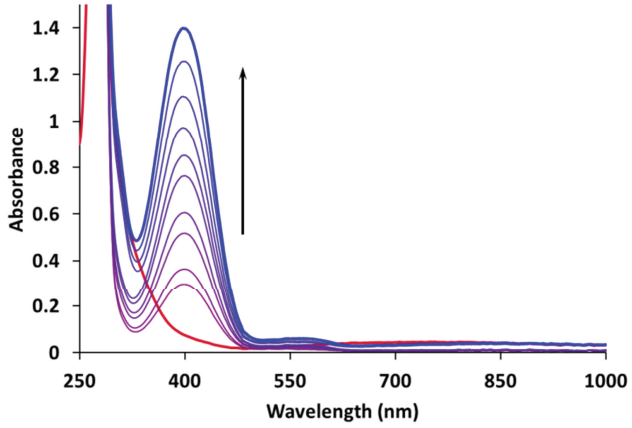

Figure AVI.4: UV-vis spectra of 3,5-DTBQ formation catalyzed by $[Cu^{II}_2(\mathbf{L}^{Pz}\mathbf{SSL}^{Pz})(Cl)_2]_n(BF_4)_{2n}$ at a concentration of 1.0 mM [Cu], 0.2 mM 3,5-DTBQ and 0.2 mM NEt_3 in CH_3CN over the course of 15 minutes. Spectra were recorded with a transmission dipprobe path length of 2.0 mm.

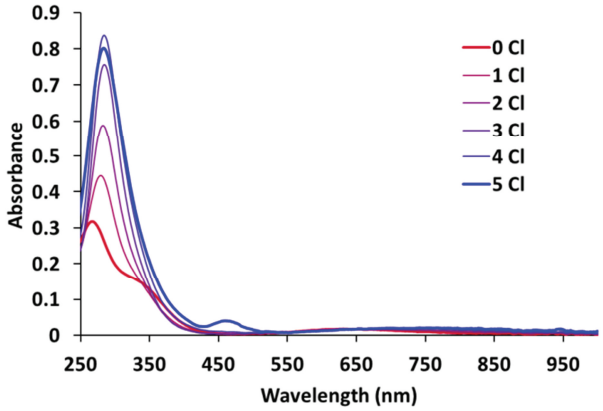

Figure AVI.5: UV-vis spectra of $[Cu^{II}_2(\mathbf{L}^{Pz}\mathbf{SSL}^{Pz})](BF_4)_4$ in CH_3CN at 1.0 mM [Cu] concentration with 0 to 5 equiv of Bu_4NCl in ratio to the whole complex. Spectra were recorded with a transmission dipprobe path length of 2.0 mm.

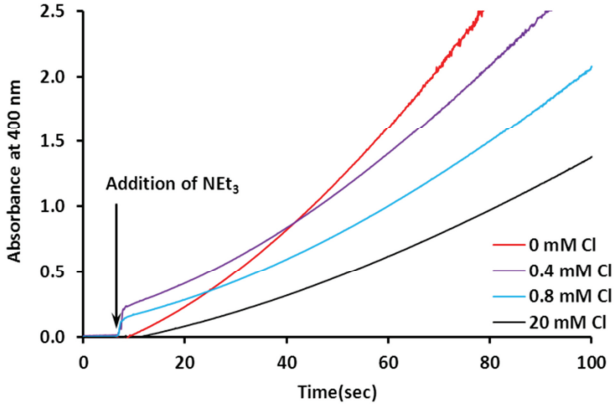

Figure AVI.6: Absorption curves at 400 nm of 3,5-DTBQ formation, catalyzed by $[Cu^{II}_2(\mathbf{L^{Pz}SSL^{Pz}})](BF_4)_4$ in the presence of 0 mM Cl^- (red), 0.4 mM Cl^- (purple), 0.8 mM Cl^- (blue) and 20 mM Cl^- (black).

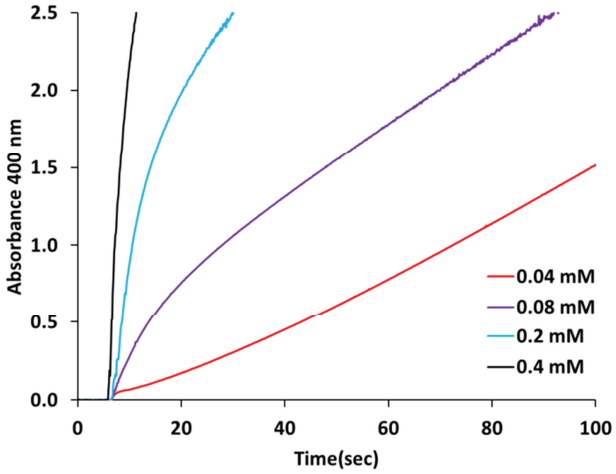

Figure AVI.7: Development in time of the absorption at 400 nm due to 3,5-DTBQ formation, catalyzed by $[Cu^{II}_2(\mathbf{L^{1*}SSL^{1*}})](BF)_4$ at different copper concentrations: 0.04 mM (red), 0.08 mM (purple), 0.2 mM (blue) and 0.4 mM (black).